

THE BROWN DWARF KINEMATICS PROJECT (BDKP). III. PARALLAXES FOR 70 ULTRACOOOL DWARFS

JACQUELINE K. FAHERTY^{1,2,9}, ADAM J. BURGASSER^{3,10}, FREDERICK M. WALTER², NICOLE VAN DER BLIEK⁴, MICHAEL M. SHARA¹,
 KELLE L. CRUZ^{1,5}, ANDREW A. WEST⁶, FREDERICK J. VRBA⁷, AND GUILLEM ANGLADA-ESCUDE⁸

¹ Department of Astrophysics, American Museum of Natural History, Central Park West at 79th Street, New York, NY 10034, USA; jfaherty@amnh.org

² Department of Physics and Astronomy, Stony Brook University, Stony Brook, NY 11794-3800, USA

³ Center of Astrophysics and Space Sciences, Department of Physics, University of California, San Diego, CA 92093, USA

⁴ CTIO/National Optical Astronomy Observatory, Chile

⁵ Department of Physics & Astronomy, Hunter College, City University of New York, 695 Park Avenue, New York, NY 10065, USA

⁶ Department of Astronomy, Boston University, 725 Commonwealth Ave Boston, MA 02215, USA

⁷ US Naval Observatory, Flagstaff Station, P.O. Box 1149, Flagstaff, AZ 86002, USA

⁸ Department of Terrestrial Magnetism, Carnegie Institution of Washington 5241 Broad Branch Road, NW, Washington, DC 20015, USA

Received 2011 September 13; accepted 2012 February 28; published 2012 May 25

ABSTRACT

We report parallax measurements for 70 ultracool dwarfs (UCDs) including 11 late-M, 32 L, and 27 T dwarfs. In this sample, 14 M and L dwarfs exhibit low surface gravity features, 6 are close binary systems, and 2 are metal-poor subdwarfs. We combined our new measurements with 114 previously published UCD parallaxes and optical–mid-IR photometry to examine trends in spectral-type/absolute magnitude, and color–color diagrams. We report new polynomial relations between spectral type and M_{JHK} . Including resolved L/T transition binaries in the relations, we find no reason to differentiate between a “bright” (unresolved binary) and a “faint” (single source) sample across the L/T boundary. Isolating early T dwarfs, we find that the brightening of T0–T4 sources is prominent in M_J where there is a [1.2–1.4] mag difference. A similar yet dampened brightening of [0.3–0.5] mag happens at M_H and a plateau or dimming of [–0.2 to –0.3] mag is seen in M_K . Comparison with evolutionary models that vary gravity, metallicity, and cloud thickness verifies that for L into T dwarfs, decreasing cloud thickness reproduces brown dwarf near-IR color–magnitude diagrams. However we find that a near constant temperature of 1200 ± 100 K along a narrow spectral subtype of T0–T4 is required to account for the brightening and color–magnitude diagram of the L-dwarf/T-dwarf transition. There is a significant population of both L and T dwarfs which are red or potentially “ultra-cloudy” compared to the models, many of which are known to be young indicating a correlation between enhanced photospheric dust and youth. For the low surface gravity or young companion L dwarfs we find that 8 out of 10 are at least [0.2–1.0] mag underluminous in M_{JH} and/or M_K compared to equivalent spectral type objects. We speculate that this is a consequence of increased dust opacity and conclude that low surface gravity L dwarfs require a completely new spectral-type/absolute magnitude polynomial for analysis.

Key words: astrometry – brown dwarfs – stars: low-mass

Online-only material: color figures, machine-readable table

1. INTRODUCTION

For any new class of astronomical objects, distances are crucial for investigating basic physical properties. Brown dwarfs, low-mass objects that lack sustained stable hydrogen burning in their cores, are a recent addition to the plethora of objects studied in astronomy. They were first predicted by Kumar (1962) and Hayashi & Nakano (1963) but not observationally confirmed until the late 1990s (Nakajima et al. 1995; Rebolo et al. 1995). They have masses between $\sim 0.072 M_\odot$ and $0.012 M_\odot$, straddling the boundary between the lowest mass stars and the highest mass exoplanets (Saumon et al. 1996; Chabrier & Baraffe 1997). In early 2000, the standard stellar spectral classification scheme was extended beyond M dwarfs to include “L” dwarfs, objects with temperatures ranging between 1300 and 2000 K and “T–Y” dwarfs, objects cooler than 1300 K (see Kirkpatrick 2005 and references therein; Cushing et al. 2011). The L-spectral class encompasses both low-mass stars and brown dwarfs, depending on the mass/age of the ultracool dwarf (UCD; see Burrows et al. 2001, and references therein).

Distances provide a direct means for calculating the luminosity and (if there is a reliable radius estimate) the effective temperature of a star or brown dwarf. Using luminosity, color, and a probe of effective temperature, brown dwarf color–magnitude diagrams can be populated and used to investigate physical and chemical parameters such as gravity, metallicity, or dust properties. Moreover, parallaxes to a significant number of objects are required to create relations with spectral type that can be used to estimate distances to the majority of brown dwarfs lacking astrometric measurements.

There are now nearly 1000 spectroscopically confirmed field L and T dwarfs¹¹ that define observational near-IR color trends. Spectroscopic standards have been designated at each subtype that exhibit characteristic features of the changing brown dwarf spectral energy distribution. The physical parameter that drives the major changes in the observable photometric and spectroscopic features of the brown dwarf population is a decreasing effective temperature (T_{eff}). However, with an ever-growing list of brown dwarfs observed in the field, a number of outliers have emerged that exhibit how secondary parameters such as age, metallicity, and cloud variability can change observable properties. There are a handful of brown dwarfs that have halo

⁹ Visiting astronomer, Cerro Tololo Inter-American Observatory, National Optical Astronomy Observatory, which are operated by the Association of Universities for Research in Astronomy, under contract with the National Science Foundation.

¹⁰ Hellman Fellow.

¹¹ According to the dwarfarchives Web site maintained at <http://dwarfarchives.org>.

Report Documentation Page

Form Approved
OMB No. 0704-0188

Public reporting burden for the collection of information is estimated to average 1 hour per response, including the time for reviewing instructions, searching existing data sources, gathering and maintaining the data needed, and completing and reviewing the collection of information. Send comments regarding this burden estimate or any other aspect of this collection of information, including suggestions for reducing this burden, to Washington Headquarters Services, Directorate for Information Operations and Reports, 1215 Jefferson Davis Highway, Suite 1204, Arlington VA 22202-4302. Respondents should be aware that notwithstanding any other provision of law, no person shall be subject to a penalty for failing to comply with a collection of information if it does not display a currently valid OMB control number.

1. REPORT DATE

10 JUN 2012

2. REPORT TYPE

3. DATES COVERED

4. TITLE AND SUBTITLE

The Brown Dwarf Kinematics Project (BDKP), III. parallaxes For 70 Ultracool Dwarfs

5a. CONTRACT NUMBER

5b. GRANT NUMBER

5c. PROGRAM ELEMENT NUMBER

6. AUTHOR(S)

5d. PROJECT NUMBER

5e. TASK NUMBER

5f. WORK UNIT NUMBER

7. PERFORMING ORGANIZATION NAME(S) AND ADDRESS(ES)

US Naval Observatory, Flagstaff Station, P.O. Box 1149, Flagstaff, AZ, 86002

8. PERFORMING ORGANIZATION
REPORT NUMBER

9. SPONSORING/MONITORING AGENCY NAME(S) AND ADDRESS(ES)

10. SPONSOR/MONITOR'S ACRONYM(S)

11. SPONSOR/MONITOR'S REPORT
NUMBER(S)

12. DISTRIBUTION/AVAILABILITY STATEMENT

Approved for public release; distribution unlimited.

13. SUPPLEMENTARY NOTES

The original document contains color images.

14. ABSTRACT

We report parallax measurements for 70 ultracool dwarfs (UCDs) including 11 late-M, 32 L, and 27 T dwarfs. In this sample, 14 M and L dwarfs exhibit low surface gravity features, 6 are close binary systems, and 2 are metal-poor subdwarfs. We combined our new measurements with 114 previously published UCD parallaxes and optical/mid-IR photometry to examine trends in spectral-type/absolute magnitude, and color-color diagrams. We report new polynomial relations between spectral type and MJHK. Including resolved L/T transition binaries in the relations we find no reason to differentiate between a ?bright? (unresolved binary) and a ?faint? (single source) sample across the L/T boundary. Isolating early T dwarfs, we find that the brightening of T0-T4 sources is prominent in MJ where there is a [1.2?1.4] mag difference. A similar yet dampened brightening of [0.3?0.5] mag happens at MH and a plateau or dimming of [8722;0.2 to 8722;0.3] mag is seen in MK. Comparison with evolutionary models that vary gravity metallicity, and cloud thickness verifies that for L into T dwarfs, decreasing cloud thickness reproduces brown dwarf near-IR color-magnitude diagrams. However we find that a near constant temperature of 1200 ? 100 K along a narrow spectral subtype of T0-T4 is required to account for the brightening and color-magnitude diagram of the L-dwarf/T-dwarf transition. There is a significant population of both L and T dwarfs which are red or potentially ?ultra-cloudy? compared to the models, many of which are known to be young indicating a correlation between enhanced photospheric dust and youth. For the low surface gravity or young companion L dwarfs we find that 8 out of 10 are at least [0.2?1.0] mag underluminous in MJH and/or MK compared to equivalent spectral type objects. We speculate that this is a consequence of increased dust opacity and conclude that low surface gravity L dwarfs require a completely new spectral-type/absolute magnitude polynomial for analysis.

15. SUBJECT TERMS

16. SECURITY CLASSIFICATION OF:			17. LIMITATION OF ABSTRACT	18. NUMBER OF PAGES 22	19a. NAME OF RESPONSIBLE PERSON
a. REPORT unclassified	b. ABSTRACT unclassified	c. THIS PAGE unclassified			

Standard Form 298 (Rev. 8-98)
Prescribed by ANSI Std Z39-18

kinematics, exhibit blue near-IR colors, and have enhanced metal hydride bands along with weakened metal oxide absorption bands indicating that they are old and metal-poor subdwarfs (Burgasser et al. 2003a, 2007; Cushing et al. 2009; Kirkpatrick et al. 2010). A number of objects have red near-IR colors, weak alkali lines, enhanced metal oxide absorption bands in the optical, and appear to be juvenile-aged members of nearby moving groups such as AB Doradus, β Pictoris, etc (Kirkpatrick et al. 2006, 2010; Cruz et al. 2009; Allers et al. 2010; Rice et al. 2010). There are also objects that do not exhibit the extreme spectral features of subdwarfs or low-gravity dwarfs, but are nevertheless near-IR photometric outliers whose photometric properties might be attributable to dust, subtle variations in age or metallicity, or photometric variability (Knapp et al. 2004; Burgasser et al. 2008b; Faherty et al. 2009; Schmidt et al. 2010; Kirkpatrick et al. 2010; Looper et al. 2008b, Radigan et al. 2012).

With the early parallax programs of Dahn et al. (2002), Tinney et al. (2003), and Vrba et al. (2004) as well as subsequent astrometric programs, the spectral-type/absolute magnitude relations and color-magnitude diagrams for brown dwarfs were first investigated (Thorstensen & Kirkpatrick 2003; Costa et al. 2006; Burgasser et al. 2008c; Lucas et al. 2010; Artigau et al. 2010; Schilbach et al. 2009; Marocco et al. 2010). One of the remarkable features of UCD color-magnitude diagrams is the significant scatter in luminosity found among objects with similar spectral types. Increasingly complex atmospheric and evolutionary models have explained this as the result of variations in secondary parameters such as gravity, metallicity, sedimentation efficiency, and/or binarity (e.g., Tsuji et al. 1996; Tsuji & Nakajima 2003; Burrows et al. 2006; Helling et al. 2008; Saumon & Marley 2008). The models disagree as to which parameter has the largest effect on the emergent spectra and color trends, and small numbers of objects with independently measured secondary parameters have hindered progress (Knapp et al. 2004; Patten et al. 2006; Leggett et al. 2010). Only by increasing the number of well-characterized UCDs with distance measurements can we hope to understand the source and extent of the variation in the color-magnitude and H-R diagrams.

Another major anomaly of brown dwarf color-magnitude diagrams is an intriguing brightening (or bump) in the J band (up to 1.5 mag; Vrba et al. 2004; Tinney et al. 2003), and to some extent H and K , as objects transition between the warmer L dwarf and cooler T dwarf spectral classes. In the past decade, several L/T transition objects have been confirmed as flux reversal binaries with resolved components straddling the bump. These objects confirm that the brightening is an intrinsic feature of brown dwarf evolution (e.g., Looper et al. 2008a; Gizis et al. 2003; Liu et al. 2006; Burgasser et al. 2006b; Burgasser 2007); however, the full extent and physical explanation remain mysterious. One possible explanation is that opacity from condensate clouds is especially influential on the $1\ \mu\text{m}$ region of L and early-type T dwarfs, so changes in cloud properties can explain the unusual brightening (e.g., Burgasser et al. 2002b; Knapp et al. 2004). The small numbers of L/T transition objects with parallax measurements has hindered progress in understanding the degree and variation in brightening exhibited at this interesting phase of brown dwarf evolution.

In late 2006, we initiated the Brown Dwarf Kinematics Project (BDKP) in order to address persistent questions of brown dwarf evolution and atmospheric properties using astrometric measurements of proper motion, parallax, and radial velocity. Proper motion analysis of the population was reported in Faherty et al.

(2009, 2010, 2011). In this work, we report parallaxes for 70 UCDs. Section 2 describes the target list as well as the data acquisition and reduction. Section 3 describes the parallax pipeline used to determine distances. Section 4 uses all parallax measurements reported in this work in combination with published values and photometric information obtained from various catalogs to investigate spectral type/absolute magnitude relations and color-magnitude diagrams for the brown dwarf population. In Section 5 an updated brown dwarf near-IR color-magnitude diagram is examined using evolutionary models. Sections 6 and 7 discuss the absolute magnitude versus spectral type relation for low surface gravity and subdwarfs, respectively. Section 8 reviews the kinematics for an ensemble of all known brown dwarfs with parallax measurements and Section 9 investigates both known and suspected binaries within the sample. Conclusions are reported in Section 10.

2. OBSERVATIONS

2.1. Target List

We compiled the parallax target list from the BDKP astrometric sample reported in Faherty et al. (2009). Instrumental limitations precluded measuring parallaxes to the faintest, most distant L and T dwarfs so we focused primarily on objects within 20 pc. However, we were also interested in subsets of the population which included low surface gravity dwarfs (potentially young sources) and subdwarfs (potentially old sources). For these scientifically interesting subsets we relaxed our astrometric constraint to include sources whose predicted spectroscopic parallax was up to 50 pc. Our full target list consisted of 70 dwarfs, including 11 M, 32 L, and 27 T dwarfs (see Table 1). In this sample there were 14 low surface gravity dwarfs, 2 subdwarfs, 6 binary systems, and 9 calibrators with previous parallax measurements.

2.2. Data Collection and Reduction

2.2.1. ANDICAM

We obtained parallax frames with the ANDICAM (A Novel Double-Imaging CAMera- DePoy 2003) imager between 2006 November and 2010 March (~ 500 hr of observations). All data were acquired through queue observing with telescope time allocated through the SMARTS (Small and Moderate Aperture Research Telescope System) consortium. ANDICAM is a dual channel near-IR and CCD imager located on the 1.3 m telescope at Cerro Tololo InterAmerican Observatory (CTIO). The optical detector is a 1024×1024 CCD and the near-IR channel uses a Rockwell 1024×1024 HgCdTe HAWAII array. The near-IR field of view is 2.4 arcmin with an unbinned plate scale of $0''.137\ \text{pixel}^{-1}$. The optical CCD field of view is larger, 6.2 arcmin, with a plate scale of $0''.369\ \text{pixel}^{-1}$. The optical and near-IR channels operate independently with a dichroic filter directing light to the two independent cameras. Therefore, we were able to take a set of near-IR images while integrating in the optical.

To ensure the same reference stars for each parallax frame, we required the target star to always be placed in the same X , Y position on the detector. We also required all observations to be made within ± 30 minutes of meridian crossing to minimize the corrections for differential color refraction (DCR, see Section 3.1 below). Typical seeing was $1''$ and useable conditions for our parallax program were up to $2''$.

Table 1
Target List

Name	SpT OPT	SpT IR	Nights	Frames ^a	Ref Stars ^a	Δt (yr)	J (MKO)	Instrument ^b	Note ^c	Flag ^d	Ref
(1)	(2)	(3)	(4)	(5)	(6)	(7)	(8)	(9)	(10)	(11)	(12)
2MASSJ00325584–4405058	L0.0 γ	–	12	49	71	2.24	14.68 \pm 0.04	A	LG		23, 22
2MASSJ00345157+0523050	–	T6.5	6	27	38	2.91	15.11 \pm 0.03	I		F	24, 19
2MASSJ0103320+193536	L6.0 β	–	6	30	54	3.08	16.16 \pm 0.08	I	LG	F	15
2MASSJ02212859–6831400	M8.0 β	–	15	60	78	2.04	13.89 \pm 0.03	A	LG		17
2MASSJ03185403–3421292	L7.0	–	8	34	46	3.08	15.44 \pm 0.05	I		F	16
SDSSJ032553.17+042540.1	–	T5.5	6	33	21	3.08	15.90 \pm 0.03	I		F	2
2MASSJ03341218–4953322	M9.0	–	16	54	73	2.96	11.32 \pm 0.02	A			77
2MASSJ04221413+1530525	M6.0 γ	–	11	39	38	2.97	12.67 \pm 0.02	A	LG		17
2MASSJ04390101–2353083	L6.5	–	14	49	58	3.00	14.31 \pm 0.03	A			3
2MASSJ04455387–3048204	L2.0	–	25	84	71	3.05	13.31 \pm 0.03	A			3
2MASSJ05012406–0010452	L4.0 γ	–	11	46	89	2.92	14.86 \pm 0.04	A	LG		17, 22,
2MASSJ05160945–0445499	–	T5.5	11	61	34	3.90	15.95 \pm 0.08	I			26, 19
2MASSJ05184616–2756457	L0.0 γ	–	10	42	42	3.14	15.16 \pm 0.04	I	LG	N	13
2MASSJ05185995–2828372	L7.5	T1.0	11	55	66	3.90	15.87 \pm 0.10	I	B		27, 16, 19
2MASSJ05361998–1920396	L1.0 β	–	9	38	59	3.14	15.65 \pm 0.08	I	LG	N	13
LHS1777	M5.0	–	21	79	32	2.84	10.15 \pm 0.02	A	Cal		78
2MASSJ06085283–2753583	M8.5 γ	–	22	80	92	3.04	13.53 \pm 0.03	A	LG		3, 79
2MASSJ06164006–6407194	sdL5.0	sdL5.0	8	28	78	3.06	16.40 \pm 0.11	I	SD	F,N	30
2MASSJ06244595–4521548	L5.0	–	17	63	86	2.27	14.36 \pm 0.03	A			17
DENIS-PJ065248.5–574137	M8.0 β	–	12	52	95	2.83	13.56 \pm 0.03	A	LG		17
2MASSJ07123786–6155528	L1.0 β	–	8	36	88	3.14	15.20 \pm 0.06	I	LG	F,N	22
2MASSJ07290002–3954043	–	T8.0	11	39	74	3.70	15.88 \pm 0.08	I			25
SDSSJ074201.41+205520.5	–	T5.0	7	19	75	2.08	15.60 \pm 0.03	I		F	9, 19
2MASSJ0746425+200032	L0.5	L1.0	13	52	91	2.69	11.64 \pm 0.03	A	B, Cal		10, 15, 9
SDSSJ083048.80+012831.1	–	T4.5	9	51	46	3.90	15.99 \pm 0.03	I			9, 19
2MASSJ08472872–1532372	L2.0	–	24	85	69	2.89	13.42 \pm 0.03	A			3
2MASSJ0859254–194926	L7.0	–	9	38	32	3.71	15.42 \pm 0.05	I			3
2MASSJ09393548–2448279	–	T8.0	8	33	63	3.81	15.61 \pm 0.09	I	B, Cal	F	31, 19
2MASSJ09490860–1545485	–	T2.0	11	61	25	3.90	16.09 \pm 0.12	I			31, 19
WT248	M3.0	–	15	63	99	2.06	10.51 \pm 0.02	A	Cal		80
2MASSJ10073369–4555147	–	T5.0	8	30	97	3.70	15.65 \pm 0.07	I		F	25
2MASSJ1010148–040649	L7.0	–	10	45	55	3.70	15.39 \pm 0.06	I			3
2MASSJ10220489+0200477	M9.0 β	–	6	34	57	3.06	14.03 \pm 0.03	I	LG	F,N	17
SDSSJ103026.78+021306.4	–	L9.5	8	41	52	3.70	17.10 \pm 0.05	I		F,N	9
2MASSWJ1036530–344138	L6.0	–	6	29	69	2.82	15.51 \pm 0.05	I		F	32
SDSSJ104335.08+121314.1	–	L7.0	7	30	63	3.71	15.82 \pm 0.03	I		F	2
SDSSJ104409.43+042937.6	–	L7.0	8	40	27	3.90	15.84 \pm 0.03	I		F	9
2MASSJ10584787–1548172	L3.0	L3.0	14	56	28	2.48	14.12 \pm 0.05	A	Cal		33, 14, 9
TWA28	M8.5 γ	–	18	67	97	2.89	12.96 \pm 0.02	A	LG		81
2MASSJ11145133–2618235	–	T7.5	9	42	42	2.08	15.52 \pm 0.05	I			31, 19
TWA26	M9.0 γ	–	15	57	90	2.22	12.61 \pm 0.03	A	LG		17
2MASSJ11553952–3727350	L2.0	–	21	91	97	2.53	12.73 \pm 0.02	A			32
SDSSJ115553.86+055957.5	–	L7.5	7	31	49	3.70	15.63 \pm 0.03	I		F	9
SDSSJ115700.50+061105.2	–	T1.5	7	37	23	3.90	17.09 \pm 0.05	I		F,N	9, 19
SDSSJ120747.17+024424.8	L8.0	T0.0	7	32	61	1.88	15.38 \pm 0.03	I		F,N	6, 19
2MASSJ12095613–1004008	T3.5	T3.0	6	30	27	3.70	15.55 \pm 0.03	I	B	F,N	24, 16, 19
2MASSJ12154432–3420591	–	T4.5	8	45	53	3.90	16.24 \pm 0.13	I		F,N	25
2MASSJ13595510–4034582	L1.0	–	15	53	98	1.80	13.58 \pm 0.03	A			17
2MASSJ14044941–3159329	T0.0	T2.5	9	35	87	3.90	15.51 \pm 0.06	I	B		25, 35
2MASSJ14442067–2019222	sdM9.0	–	15	63	87	2.87	12.51 \pm 0.02	A	SD, Cal		72, 82
SDSSpJ14460060+002452.0	L6.0	L5.0	7	36	52	2.08	15.56 \pm 0.05	I	Cal	F,N	34, 6, 9
SDSSJ150411.63+102718.4	–	T7.0	9	39	66	2.08	16.49 \pm 0.03	I			2
SDSSJ151114.66+060742.9	–	T0.0	8	46	43	2.08	15.83 \pm 0.03	I	B	F	2
SDSSJ152103.24+013142.7	–	T2.0	6	38	41	2.08	16.06 \pm 0.03	I		F	9, 19
2MASSJ1526140+204341	L7.0	–	6	23	73	1.88	15.48 \pm 0.05	I		F	15
2MASSJ16150413+1340079	–	T6.0	8	33	86	2.08	16.32 \pm 0.09	I		F	25
SDSSJ163022.92+081822.0	–	T5.5	6	25	73	1.88	16.18 \pm 0.03	I		F,N	2
2MASSJ16452211–1319516	L1.5	–	12	47	99	1.16	12.37 \pm 0.03	A			32
2MASSJ17545447+1649196	–	T5.5	5	11	98	1.88	15.79 \pm 0.07	I		F	1
2MASSJ18283572–4849046	–	T5.5	9	39	93	1.88	15.17 \pm 0.06	I			24, 19
2MASSJ19360187–5502322	L5.0	–	13	37	97	1.31	14.40 \pm 0.04	A			17
SDSSJ204749.61–071818.3	–	T0.0	6	22	79	1.34	16.70 \pm 0.03	I		F	9, 19
SDSSJ205235.31–160929.8	–	T1.0	6	13	71	1.88	16.04 \pm 0.03	I	B	F,N	2
2MASSJ20575409–0252302	L1.5	L1.5	20	75	93	2.20	13.04 \pm 0.02	A			3, 7

Table 1
(Continued)

Name	SpT OPT	SpT IR	Nights	Frames ^a	Ref Stars ^a	Δt (yr)	J (MKO)	Instrument ^b	Note ^c	Flag ^d	Ref
(1)	(2)	(3)	(4)	(5)	(6)	(7)	(8)	(9)	(10)	(11)	(12)
2MASSJ21321145+1341584	L6.0	—	5	19	75	1.20	15.68 \pm 0.06	I	B	F,N	13
2MASSJ21513839+4853542	—	T4.0	7	29	72	1.52	15.71 \pm 0.07	I		F	38,19
2MASSJ22282889+4310262	—	T6.0	7	29	52	3.47	15.64 \pm 0.07	I		F	26,19
2MASSJ23224684+3133231	L0.0 β	—	9	34	66	1.39	13.50 \pm 0.03	A	LG		17
2MASSJ2356547+155310	—	T5.5	7	27	46	3.47	15.48 \pm 0.03	I	Cal	F	36,19
2MASSJ23594034+7335055	—	T5.5	9	42	55	3.47	16.10 \pm 0.10	I			1

Notes.^a Number of frames and reference stars used in the parallax solution.^b I: ISPI and A: ANDICAM.^c LG is a low surface gravity dwarf, Cal is a calibrator ultracool dwarf, SD is an ultracool subdwarf, B is a tight binary unresolved in 2MASS.^d F indicates an object with <9 parallax frames; N indicates an object with M_{JHK} uncertainties >0.5 mag therefore; unless otherwise noted, it indicates that the target was not used in the analysis throughout the paper.

References. (1) This paper; (2) Chiu et al. (2006); (3) Cruz et al. 2003; (4) Gizis et al. 2000; (5) Golimowski et al. 2004; (6) Hawley et al. 2002; (7) Kendall et al. 2004; (8) Kirkpatrick et al. 1997; (9) Knapp et al. 2004; (10) Reid et al. 2000; (11) Ruiz et al. 1997; (12) Wilson et al. 2001; (13) Cruz et al. 2007; (14) Kirkpatrick et al. 1999; (15) Kirkpatrick et al. 2000; (16) Kirkpatrick et al. 2008; (17) Reid et al. 2008; (18) Forveille et al. 2004; (19) Burgasser et al. 2006a; (20) Burgasser et al. 2008a; (21) Stumpf et al. 2008; (22) Cruz et al. 2009; (23) EROS Collaboration et al. 1999; (24) Burgasser et al. 2003d; (25) Looper et al. 2007; (26) Burgasser et al. 2004; (27) Cruz et al. 2004; (28) Burgasser et al. 2000b; (29) Burgasser et al. 2003b; (30) Cushing et al. 2009; (31) Tinney et al. 2005; (32) Burgasser et al. 2002a; (33) Delfosse et al. 1997; (34) Geballe et al. 2002; (35) Looper et al. 2008a; (36) Burgasser et al. 2002a; (37) Lépine et al. 2003a; (38) Ellis et al. 2005; (39) Martin et al. 1999; (40) Thorstensen & Kirkpatrick 2003; (41) Burgasser et al. 2004; (42) Fan et al. 2000; (43) Burgasser et al. 2003a; (44) Scholz et al. 2003; (45) Leggett et al. 2000; (46) Luhman et al. 2007; (47) Lodieu et al. 2007; (48) Biller et al. 2006; (49) Strauss et al. 1999; (50) Burgasser et al. 1999; (51) Artigau et al. 2010; (52) Tsvetanov et al. 2000; (53) Nakajima et al. 1995; (54) Mugrauer et al. 2006; (55) Pinfield et al. 2008; (56) Burgasser et al. 2000a; (57) Goldman et al. 2010; (58) Burningham et al. 2009; (59) Warren et al. 2007; (60) Delorme et al. 2008; (61) Burningham et al. 2008; (62) Lucas et al. 2010; (63) Schneider et al. 2002; (64) Burgasser et al. 2007; (65) Kirkpatrick et al. 2001; (66) Kasper et al. 2007; (67) Burgasser et al. 2010b; (68) Costa et al. 2006; (69) Dahn et al. 2002; (70) Henry et al. 2006; (71) Perryman et al. 1997; (72) Schilbach et al. 2009.

In the optical we observed in the I_c band with integration times that ranged from 265 s for our brightest targets to 610 s for our faintest (typical S/N > 100 for all targets). In the near-IR we observed in the J band with integration times that ranged from 20 s with 5 co-adds for our brightest targets to 130 s with 8 co-adds for our faintest. We acquired 5–7 near-IR images in a 10'' dither pattern.

The optical ANDICAM data were processed with overscan subtraction and flat-fielding, prior to distribution. Initially we intended to use the near-IR data for parallaxes and the CCD data as a check on the astrometric quality. However, we quickly realized that the optical images were far superior to the near-IR, which were plagued with imaging artifacts, an occasional elongated point spread function (PSF), and a smaller field of view (therefore fewer reference stars). As a result we report parallaxes in this paper based only on the optical imaging.

2.2.2. Infrared Side Port Imager (ISPI)

We collected parallax data for our faintest targets with the Infrared Side Port Imager (ISPI) on the CTIO 4 m Blanco telescope (van der Blik et al. 2004). ISPI is a 2048 \times 2048 HgCdTe HAWAII-2 array with an \sim 8 arcmin field of view and nominal plate scale of 0''.303 pixel⁻¹. Observations were conducted over a period of just under 2 yr (from early 2008 March through late 2010 April) on 15 observing runs. After the spring of 2010, ISPI was replaced on the Blanco 4 m telescope with the NEWFIRM infrared detector. However, it was put back on the telescope in October of 2011 and we obtained three more epochs over six nights of observing in 2011 November, 2012 January, and 2012 February. These new parallax frames are also included in this work.

As opposed to ANDICAM, ISPI data were collected classically. All observations were carried out in the J band

under seeing conditions up to 2'' FWHM with typical conditions between 0''.8 and 1''.1. Most of the parallax observations were made when the target was within \pm 30 minutes of the meridian to minimize the corrections for DCR (see Section 3.1 below). However, due to observational constraints (weather, instrument issues, etc.) some targets were observed within \pm 1 hr of meridian crossing.

In order to minimize the effects of distortion and to ensure the same reference stars in each frame, we placed the target star on the same X, Y pixel position for each parallax frame. On the first observing run for a target, the frame was initially offset from the center of the chip to avoid the four-quadrant seam along the detector. This initial frame was used in all subsequent observing runs as a reference for determining where to place the parallax star.

Integration times were set by the magnitude of the target and the conditions at the telescope. They ranged from 30 to 60 s with 5–10 co-adds and 5–10 images in a 10'' dither pattern (typical S/N > 100 for all targets). Depending on the weather and seeing conditions, the typical integration time per target was 15–40 minutes.

Dark frames and lights on/off dome flats were obtained at the start of each evening. Reduction procedures were based on the prescriptions put together by the ISPI team¹² utilizing a combination of IRAF routines. J -band flats were created by median combining the lights on and lights off images then subtracting the two. Bad pixel masks were created from a dome flat image. Individual parallax frames were flat-fielded and corrected for bad pixels with the calibration images. All images were flipped to orient north up and east to the left using the IRAF routine *osiris* in the *cirred* package. Finally, the IRAF

¹² http://www.ctio.noao.edu/instruments/ir_instruments/ispi/

routine *xdimsum* was used to perform sky subtractions and mask holes from bright stars.¹³

3. PARALLAX PIPELINE

3.1. Source Extraction

Once all images were reduced, we used the Carnegie Astrometric Planet Search (hereafter ATPa) software to extract all point sources and solve for relative parallaxes and proper motions (Boss et al. 2009). Images were not co-added; rather, sources were extracted on every image at every dither position.

The processing of each night of observation (or epoch) was treated separately and consisted of extracting the position of all point sources. This required the specification of (1) a guess of the FWHM of each set of images, (2) the plate scale for the instrument, and (3) a high quality image to be used as the template used to generate a preliminary list of sources to be extracted on all other frames in a given epoch.

The precise centroids of the stars were measured by binning the stellar profile in the X and Y directions using a box of $\sim 2''$ around the pixel with maximum flux. Each one-dimensional profile was precisely centroided by finding the zero of the profile convolution using *Tukey's biweight function* (Tukey 1977). The width of this function depends on a scale parameter to compute the centroid which was varied and the average taken (FWHM -0.5 pixel, FWHM -0.25 pixel, FWHM, FWHM $+0.25$ pixel, FWHM $+0.5$ pixel) to mitigate systematic effects caused by poor sampling of the stellar PSF. We tested a variety of centroiding methods using different profiles but decided that the convolution approach described above provided the best centroid accuracy and robustness (see Boss et al. 2009 for further details). Once all sources were extracted on all the frames in a given night, the 10 stars showing the best formal centroid uncertainties were used to define a preliminary reference frame and their standard deviation assigned as the precision per image.

ATPa generates a text file (from now on referred to as a plate file) containing X , Y positions with corresponding uncertainties (in pixels), and a rough flux measurement of all the successfully extracted stars. Plate files were used in the next step of the processing to calibrate the field distortions and measure the motion of each star as a function of time. Objects displaying positional uncertainties larger than 5 times the median precision were automatically removed. These were usually spurious sources caused by unfiltered detector artifacts or cosmic rays. The typical centroiding uncertainty for parallax targets in ISPI and ANDICAM was ~ 0.01 pixels.

DCR corrections are typically required because the parallax star and reference stars have very different colors. As a result, their positions shift relative to one another due to different amounts of atmospheric refraction. The effect is wavelength, weather, and zenith-distance dependent. Stone (1996, 2002) presents a theoretical method for determining DCR effects. That work demonstrates that by maintaining small zenith distances, DCR effects in I and longer wavelengths (such as J) are minimal, typically < 1 mas. Similar results were found using the empirical methodology proposed by Monet et al. (1992). The low-mass star optical parallax program of Jao et al. (2005) and the brown dwarf optical parallax program of Dahn et al. (2002) also

found negligible I -band DCR corrections as did the near-IR T dwarf parallax program of Tinney et al. (2003). Therefore, DCR corrections are not applied to the positions in our pipeline. To ensure that even this small effect was minimized, we observed targets (with few exceptions) within ± 30 minutes of meridian crossing.

3.2. Astrometric Solution and Parallax

Using the *Astrometric Iterative Solution* included in the ATPa package, the extracted X , Y pixel positions were mapped to a local tangent plane in order to solve for the astrometric parameters. The highest quality image obtained for a given parallax target was designated as the initial catalog to which everything was matched in the first astrometric iteration. The solution needed to be initialized with the right ascension (R.A.) and declination (decl.) coordinates of the brightest star in the field; however, the coordinates were only required to compute the projected parallax motion in the tangent plane. Therefore a precision of a few arcseconds on this bright star was more than sufficient to initialize the solution. In the first iteration, the position of the stars in the initial catalog were still approximate, so only a linear transformation was applied to each plate to correct for telescope pointing, field rotation, and changes in the plate scale. This matching provided the position of each star as a function of time in the reference frame defined by the initial catalog. The apparent trajectory of each star was then fit to a linearized astrometric model

$$x(t) = x_0 + \mu_\alpha(t - t_0) - \Pi p_\alpha(t), \quad (1)$$

$$y(t) = y_0 + \mu_\delta(t - t_0) - \Pi p_\delta(t), \quad (2)$$

where x_0 and y_0 are positional offsets at the first epoch of observation t_0 ; μ_α and μ_δ are the proper motion in R.A. and decl., respectively; Π is the parallax; and p_α and p_δ are the parallax factors in R.A. and decl., respectively. At this point, all the quantities are given in milliarcseconds (mas) and the time t is measured in years. The parallax factors are computed using the Earth geocenter as obtained from the DE405 Ephemeris.¹⁴ This linearized model is based on the prescriptions laid out in the *HIPPARCOS* (Perryman et al. 1997) and *Tycho* Catalogues¹⁵ (Hog et al. 2000).

After the astrometric solution of the field was obtained, a subset of well-behaved stars (rms < 5 mas and at least 4–5 observations) was chosen and the second iteration begun using those as reference sources. The whole process (crossmatching, field distortion fit, and astrometric solution) was repeated a number of times. After the first iteration, ATPa allowed fitting more detailed field distortion corrections using higher order polynomials in X and Y . We tested up to third-order polynomials but these yielded negligible improvement in both ANDICAM and ISPI images. Consequently, we ran all targets using a second-order polynomial.

We set the number of total iterations to 3–5. The convergence was monitored by checking the average rms of the well-behaved reference sources. This iterative process was automated by ATPa and required little supervision. The selection of reference stars was done automatically, but ATPa allowed the user to flag problematic reference stars. As a result, after a first solution was obtained, we checked the final catalog and re-ran the whole

¹³ We note that during observations the primary mirror would occasionally vibrate causing the PSF to appear elongated. When this occurred we would halt and restart an integration. The problem was sporadic but did not affect any of the final images.

¹⁴ <http://ssd.jpl.nasa.gov/>

¹⁵ http://www.rssd.esa.int/SA/HIPPARCOS/docs/vol1_all.pdf

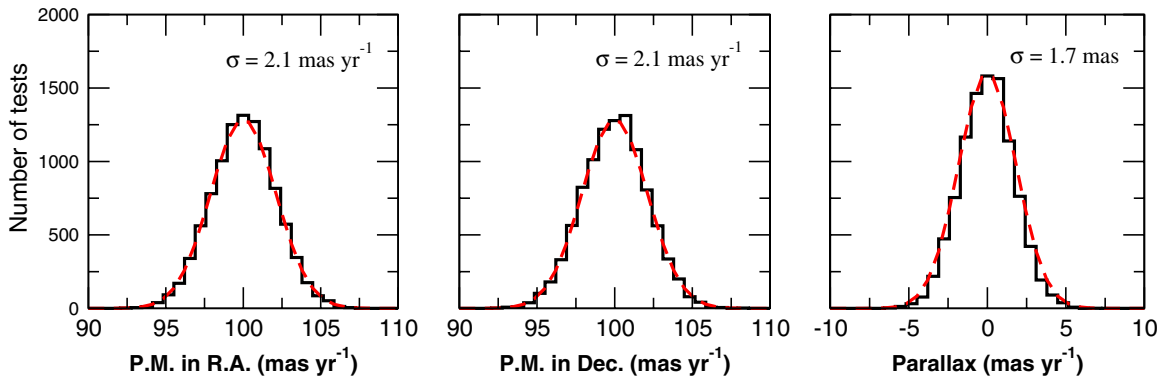


Figure 1. Histograms (black) of the obtained distributions from 10^5 synthetic data sets obtained using the epochs for calibrator 2M0746+2000. Each simulated data set assumes a 0 parallax and $+100 \text{ mas yr}^{-1}$ in both R.A. and decl. The red dashed line is a Gaussian distribution with σ equal to the standard deviation measured on the Monte Carlo generated data sets, illustrating the perfect agreement between the two, and validating our approach to determine empirical uncertainties.

(A color version of this figure is available in the online journal.)

astrometric process eliminating the following objects from the reference frame: (1) the target parallax star, (2) other high proper motion stars in the field, (3) saturated stars, and (4) elongated or extended sources (e.g., galaxies). The whole iterative process was repeated a second time. The final catalog that was output by ATPa contained the five free parameters defined above for each star in the field. It also contained formal uncertainties derived from the covariance matrix of the least-squares solution for the equations above, information about the number of observations employed, and the rms of the residuals per epoch.

In Table 1 we list the data on each target including the baseline between the first and last observations, the number of nights a target was observed (epochs), and how many parallax frames were included in the solution. In the case of a number of targets, parallactic sampling was low (e.g., 5–7 epochs); therefore, to ensure realistic uncertainties, we applied a Monte Carlo method to the solution. For each target, we independently measured the standard deviation of the R.A. and decl. residuals. However, since many of the targets had a small number of epochs, we used the median standard deviation from the reference stars instead. These more realistic residuals were used to add random Gaussian noise to simulated observations with the parallax and proper motion from the final ATPa catalog. We repeated this experiment 1000 times and solved for the five astrometric parameters each time. The standard deviation around the mean value of the parallax over the Monte Carlo runs is the final uncertainty listed in Table 2. As long as the standard deviations used in the Monte Carlo experiment are realistic, this approach automatically accounts for the correlation between the parallax and proper motion and offsets the issue of undersampled astrometry. We flag sources in Table 1 that have <9 epochs and potentially undersampled parallaxes.

We note that parallax and proper motion are linear parameters of the model. As a consequence, one does not depend on the particular value of the other in any way. Still, it is true that they can be correlated due to the sampling cadence. One of the advantages of the Monte Carlo approach used here is that such a correlation is automatically accounted for in the process of generating synthetic data sets at the same observing epochs and deriving the empirical standard deviations over the repetitions of the same measurement. To illustrate this, we use the observing epochs of 2M0746+2000 (13 epochs over 2.5 yr) and simulate astrometric measurements assuming 0 parallax and a proper motion of $+100 \text{ mas yr}^{-1}$ on both R.A. and decl. We introduce random Gaussian noise with a standard deviation of

5 mas in both R.A. and decl. and solve for all the astrometric parameters. We repeat this experiment 10,000 times and produce the numerical distributions of the obtained μ_α , μ_δ , and parallax. As expected from a linear model, the obtained distributions are non-biased and the shape of the marginalized distributions is Gaussian with the same σ we measure on the scatter of the 10^5 Monte Carlo obtained parameters (see Figure 1).

3.3. Correction from Relative to Absolute Parallax

The final parallaxes from the astrometric solution are relative to the motion of the background stars chosen as references. A correction is required based upon the true parallaxes of the reference stars to convert to an absolute measurement.

Typically there are three ways to convert from relative to absolute parallaxes: (1) using statistical methods that rely on a well-determined model of the Galaxy and is most relevant for faint distant reference stars, (2) spectroscopic parallaxes that rely on spectral data obtained for every reference star, or (3) photometric parallaxes that rely on colors for all reference stars. We determined the parallax corrections using the third method because the reference stars are primarily the brightest in the field and spectral data are not available.

In order to measure photometric parallaxes for the reference stars we assume that all sources are main-sequence dwarfs. Following a similar procedure described in Vrba et al. (2004), we obtained 2MASS photometry for all reference stars. We compared with the intrinsic colors described in Koornneef (1983) so we first converted J, H, K_s values to the Koornneef photometric system using the transformations detailed in Carpenter (2001). The near-IR $J - H$ and $H - K$ colors were used to estimate spectral types and $V - K$ colors of the background stars based on the relations detailed in Koornneef (1983) for main-sequence dwarfs. Absolute V magnitudes were taken from color spectral type relations described in Kitchin (2004) and then converted to M_J and M_K values. Distances to reference stars were determined by averaging $(m - M)_J$ and $(m - M)_K$ values which were in good agreement.

Each reference star was given equal weight in the astrometric solution. As a result we averaged the photometric parallaxes to calculate the distance correction and used a standard deviation of the mean for the correction uncertainty. We added the distance correction to our relative parallax and added the correction uncertainty in quadrature with our parallax uncertainty to obtain the final absolute parallax. The average correction to absolute

Table 2
Astrometry of Targets

Name	SpT	π_{rel} (mas)	π_{abs} (mas)	μ_{α} (mas yr ⁻¹)	μ_{δ} (mas yr ⁻¹)	V_{tan} (km s ⁻¹)
(1)	(2)	(3)	(4)	(5)	(6)	(7)
2MASSJ00325584-4405058	L0 γ	36.6 \pm 4.6	38.4 \pm 4.8	117.8 \pm 4.3	-91.6 \pm 4.3	18.4 \pm 2.8
2MASSJ00345157+0523050	T6.5	103.3 \pm 7.2	105.4 \pm 7.5	658.8 \pm 6.2	181.0 \pm 6.0	30.8 \pm 1.2
2MASSJ0103320+193536	L6 β	45.2 \pm 7.5	46.9 \pm 7.6	293.0 \pm 4.6	27.7 \pm 4.7	29.8 \pm 4.2
2MASSJ02212859-6831400	M8 β	23.7 \pm 3.3	25.4 \pm 3.6	53.9 \pm 4.4	13.7 \pm 4.5	10.4 \pm 2.9
2MASSJ03185403-3421292	L7	70.2 \pm 7.3	72.9 \pm 7.7	391.7 \pm 6.4	34.1 \pm 6.5	25.6 \pm 2.0
SDSSJ032553.17+042540.1	T5.5	52.9 \pm 10.8	55.6 \pm 10.9	-163.7 \pm 5.8	-59.6 \pm 5.7	14.9 \pm 3.3
2MASSJ03341218-4953322	M9	119.1 \pm 3.4	120.6 \pm 3.6	2329.5 \pm 4.2	553.6 \pm 4.3	94.2 \pm 0.8
2MASSJ04221413+1530525	M6 γ	22.2 \pm 2.9	24.8 \pm 3.1	-17.2 \pm 2.7	7.4 \pm 2.6	3.6 \pm 1.5
2MASSJ04390101-2353083	L6.5	108.8 \pm 3.8	110.4 \pm 4.0	-116.3 \pm 3.8	-162.0 \pm 3.8	8.6 \pm 0.3
2MASSJ04455387-3048204	L2	75.9 \pm 2.7	78.5 \pm 4.9	164.0 \pm 2.8	-415.0 \pm 2.7	27.0 \pm 1.2
2MASSJ05012406-0010452	L4 γ	75.2 \pm 4.7	76.4 \pm 4.8	182.4 \pm 4.3	-132.7 \pm 4.2	14.0 \pm 0.9
2MASSJ05160945-0445499	T5.5	42.5 \pm 6.4	44.5 \pm 6.5	-202.7 \pm 3.6	-190.1 \pm 3.6	29.6 \pm 3.9
2MASSJ05184616-2756457	L0 γ	19.8 \pm 6.8	21.4 \pm 6.9	28.6 \pm 4.2	-16.0 \pm 4.0	7.3 \pm 6.6
2MASSJ05185995-2828372	L7.5	46.2 \pm 6.8	47.5 \pm 6.8	-76.5 \pm 4.0	-272.7 \pm 4.1	28.3 \pm 3.6
2MASSJ05361998-1920396	L1 β	24.0 \pm 9.3	25.6 \pm 9.4	24.6 \pm 5.3	-30.6 \pm 5.0	7.3 \pm 7.1
LHS1777	M5	77.4 \pm 2.1	79.9 \pm 2.5	-175.6 \pm 2.2	937.9 \pm 2.3	56.6 \pm 0.8
2MASSJ06085283-2753583	M8.5 γ	30.9 \pm 3.5	32.0 \pm 3.6	8.9 \pm 3.5	10.7 \pm 3.5	2.1 \pm 0.9
2MASSJ06164006-6407194	sdL5	18.1 \pm 6.3	19.9 \pm 6.5	1304.0 \pm 3.9	-31.9 \pm 3.7	311.7 \pm 45.5
2MASSJ06244595-4521548	L5	83.2 \pm 4.5	83.9 \pm 4.5	-41.0 \pm 5.4	355.3 \pm 5.1	20.2 \pm 0.8
DENIS-PJ065248.5-574137	M8 β	30.1 \pm 3.1	31.3 \pm 3.2	0.1 \pm 3.4	29.2 \pm 3.3	4.4 \pm 1.2
2MASSJ07123786-6155528	L1 β	21.2 \pm 9.0	22.9 \pm 9.1	-35.7 \pm 4.9	79.1 \pm 4.8	17.9 \pm 13.2
2MASSJ07290002-3954043	T8	123.4 \pm 8.1	126.3 \pm 8.3	-566.6 \pm 5.3	1643.4 \pm 5.5	65.3 \pm 1.5
SDSSJ074201.41+205520.5	T5	65.1 \pm 8.5	66.5 \pm 8.6	-311.5 \pm 8.7	-227.9 \pm 8.7	27.6 \pm 2.7
2MASSJ0746425+200032	L0.5	84.8 \pm 4.5	86.2 \pm 4.6	-355.9 \pm 5.1	-63.7 \pm 5.2	19.9 \pm 0.8
SDSSJ083048.80+012831.1	T4.5	41.2 \pm 5.9	43.1 \pm 6.1	188.9 \pm 3.0	-351.5 \pm 2.9	43.9 \pm 4.6
2MASSJ08472872-1532372	L2	75.4 \pm 3.5	76.5 \pm 3.5	131.3 \pm 3.9	-199.0 \pm 3.9	14.8 \pm 0.6
2MASSJ0859254-194926	L7	64.2 \pm 6.1	65.4 \pm 6.1	-324.5 \pm 3.7	-94.7 \pm 3.5	24.5 \pm 1.8
2MASSJ09393548-2448279	T8	194.6 \pm 10.4	196.0 \pm 10.4	558.1 \pm 5.8	-1030.5 \pm 5.6	28.4 \pm 0.6
2MASSJ09490860-1545485	T2	53.2 \pm 6.4	55.3 \pm 6.6	-98.1 \pm 2.9	8.9 \pm 2.9	8.4 \pm 1.5
WT248	M3	30.6 \pm 4.6	31.7 \pm 4.7	-1199.4 \pm 5.9	-140.5 \pm 5.8	180.6 \pm 11.3
2MASSJ10073369-4555147	T5	69.6 \pm 5.1	71.0 \pm 5.2	-723.5 \pm 3.4	148.7 \pm 3.6	49.3 \pm 1.9
2MASSJ1010148-040649	L7	58.5 \pm 8.1	59.8 \pm 8.1	-308.7 \pm 4.9	-9.7 \pm 4.8	24.5 \pm 2.8
2MASSJ10220489+0200477	M9 β	25.0 \pm 11.4	26.4 \pm 11.5	-156.2 \pm 6.6	-429.0 \pm 6.8	82.1 \pm 29.8
SDSSJ103026.78+021306.4	L9.5	23.6 \pm 10.6	24.8 \pm 10.6	50.0 \pm 5.3	62.0 \pm 4.8	15.3 \pm 13.1
2MASSWJ1036530-344138	L6	59.8 \pm 8.9	61.5 \pm 9.1	-13.3 \pm 6.7	-486.6 \pm 5.9	37.5 \pm 3.7
SDSSJ104335.08+121314.1	L7	66.8 \pm 10.6	68.5 \pm 10.6	26.0 \pm 5.1	-234.2 \pm 3.9	16.3 \pm 2.5
SDSSJ104409.43+042937.6	L7	50.0 \pm 10.0	51.3 \pm 10.1	-29.6 \pm 4.3	89.7 \pm 3.4	8.7 \pm 2.7
2MASSJ10584787-1548172	L3	64.2 \pm 3.9	66.5 \pm 4.4	-253.5 \pm 3.4	39.7 \pm 3.2	18.3 \pm 1.1
TWA28	M8.5 γ	26.4 \pm 4.2	28.0 \pm 4.3	-55.7 \pm 3.9	-7.4 \pm 3.8	9.5 \pm 2.9
2MASSJ11145133-2618235	T7.5	175.1 \pm 7.0	176.8 \pm 7.0	-2927.2 \pm 7.0	-374.2 \pm 7.2	79.2 \pm 0.8
TWA26	M9 γ	33.6 \pm 4.2	35.1 \pm 4.3	-75.2 \pm 4.4	-10.4 \pm 4.5	10.3 \pm 2.1
2MASSJ11553952-3727350	L2	102.8 \pm 4.6	104.4 \pm 4.7	66.8 \pm 4.8	-777.9 \pm 4.7	35.5 \pm 0.8
SDSSJ115553.86+055957.5	L7.5	56.6 \pm 10.2	57.9 \pm 10.2	-420.5 \pm 6.1	-54.5 \pm 4.8	34.7 \pm 4.5
SDSSJ115700.50+061105.2	T1.5	31.4 \pm 14.2	33.8 \pm 14.2	158.9 \pm 7.1	-121.3 \pm 6.5	28.0 \pm 14.7
SDSSJ120747.17+024424.8	L8	42.3 \pm 12.2	44.5 \pm 12.2	-487.0 \pm 12.9	140.1 \pm 11.7	54.1 \pm 10.4
2MASSJ12095613-1004008	T3	45.9 \pm 11.1	47.3 \pm 11.1	268.8 \pm 7.0	-356.7 \pm 5.7	44.8 \pm 7.7
2MASSJ12154432-3420591	T4.5	38.5 \pm 8.9	39.8 \pm 8.9	-223.7 \pm 5.6	-344.8 \pm 5.2	48.9 \pm 8.3
2MASSJ13595510-4034582	L1	62.8 \pm 5.4	64.2 \pm 5.5	64.6 \pm 7.7	-494.1 \pm 6.7	36.8 \pm 2.1
2MASSJ14044941-3159329	T2.5	38.5 \pm 6.1	40.0 \pm 6.2	334.5 \pm 4.9	-15.5 \pm 4.7	39.7 \pm 5.0
2MASSJ14442067-2019222	sdM9	59.7 \pm 4.9	61.2 \pm 5.1	-2905.1 \pm 3.4	-1953.9 \pm 3.4	271.3 \pm 5.5
SDSSpJ14460060+002452.0	L6	45.2 \pm 14.5	46.7 \pm 14.6	202.9 \pm 10.9	-100.4 \pm 10.8	23.0 \pm 7.7
SDSSJ150411.63+102718.4	T7	51.2 \pm 7.1	52.5 \pm 7.1	373.8 \pm 7.9	-322.5 \pm 7.7	44.6 \pm 4.0
SDSSJ151114.66+060742.9	T0	35.4 \pm 6.4	36.7 \pm 6.4	-255.6 \pm 7.1	-238.0 \pm 7.5	45.1 \pm 6.3
SDSSJ152103.24+013142.7	T2	40.2 \pm 7.2	41.3 \pm 7.2	-174.3 \pm 7.7	83.7 \pm 7.7	22.2 \pm 4.2
2MASSJ1526140+204341	L7	47.1 \pm 8.6	48.5 \pm 8.7	-206.6 \pm 10.1	-349.8 \pm 9.0	39.7 \pm 5.3
2MASSJ16150413+1340079	T6	67.2 \pm 6.3	68.6 \pm 6.4	257.8 \pm 7.9	-321.9 \pm 7.9	28.5 \pm 1.9
SDSSJ163022.92+081822.0	T5.5	45.4 \pm 10.1	46.9 \pm 10.1	-75.5 \pm 12.5	-100.0 \pm 12.1	12.7 \pm 3.7
2MASSJ16452211-1319516	L1.5	107.6 \pm 5.7	109.9 \pm 6.1	-347.7 \pm 11.5	-777.2 \pm 10.4	36.8 \pm 1.0
2MASSJ17545447+1649196	T5.5	86.0 \pm 10.2	87.6 \pm 10.2	113.5 \pm 9.1	-141.4 \pm 9.2	9.8 \pm 1.3
2MASSJ18283572-4849046	T5.5	81.0 \pm 7.1	83.7 \pm 7.7	231.4 \pm 10.5	52.4 \pm 10.9	13.4 \pm 1.2
2MASSJ19360187-5502322	L5	64.9 \pm 5.4	66.3 \pm 5.4	234.7 \pm 9.0	-289.3 \pm 9.3	26.6 \pm 1.7
SDSSJ204749.61-071818.3	T0	48.5 \pm 7.8	49.9 \pm 7.9	48.7 \pm 11.4	-193.8 \pm 11.2	19.0 \pm 3.2
SDSSJ205235.31-160929.8	T1	25.2 \pm 9.1	26.8 \pm 9.1	410.4 \pm 10.9	170.4 \pm 9.7	78.7 \pm 20.9
2MASSJ20575409-0252302	L1.5	68.4 \pm 3.6	70.1 \pm 3.7	1.6 \pm 3.8	-86.3 \pm 3.9	5.8 \pm 0.5

Table 2
(Continued)

Name	SpT	π_{rel} (mas)	π_{abs} (mas)	μ_{α} (mas yr ⁻¹)	μ_{δ} (mas yr ⁻¹)	V_{tan} (km s ⁻¹)
(1)	(2)	(3)	(4)	(5)	(6)	(7)
2MASSJ21321145+1341584	L6	28.3 ± 8.0	30.0 ± 8.2	16.4 ± 11.6	−141.0 ± 11.2	22.4 ± 8.0
2MASSJ21513839−4853542	T4	48.7 ± 6.6	50.4 ± 6.7	408.8 ± 9.9	−196.2 ± 9.0	42.7 ± 4.0
2MASSJ22282889−4310262	T6	92.7 ± 7.0	94.0 ± 7.0	102.3 ± 5.8	−324.4 ± 5.1	17.2 ± 1.0
2MASSJ23224684−3133231	L0 β	57.6 ± 5.5	58.6 ± 5.6	−194.8 ± 7.4	−527.3 ± 7.5	45.5 ± 2.7
2MASSJ2356547−155310	T5.5	71.7 ± 4.4	74.4 ± 5.8	−422.7 ± 4.0	−615.9 ± 3.6	47.7 ± 2.0
2MASSJ23594034−7335055	T5.5	85.4 ± 5.7	86.7 ± 5.7	280.9 ± 5.4	39.2 ± 5.5	15.5 ± 0.9

parallax for the full list of targets was 1.5 ± 0.5 mas ranging from 0.8 to 2.9 mas. The final parallaxes with absolute corrections are shown in Table 2.

3.4. Comparison of Calibrators

There are nine calibrator stars in our full astrometric sample (three imaged with ISPI and six imaged with ANDICAM) that we obtained as a check on the reliability of our methods. Table 3 lists the astrometry for the calibrators measured in this work and compares those values with results reported in the literature (see Figure 2). Of the nine calibrators, seven match within 1σ and all but one (TWA 28) match within 2σ of published values. No systematic trends were detected in the parallax measurement differences. The mean difference and scatter between literature and BDKP values is -4.0 ± 5.0 mas. This indicates that our parallax pipeline produces reliable results.

As a check on non-calibrator stars we examined how well the proper motion values match published values for all sources in our sample. The two lower panels in Figure 2 show plots of μ_{α} and μ_{δ} from the literature versus our calculated values with uncertainties. We find that 42% of the sample match both components within 1σ , 76% match within 2σ , 87% match within 3σ , and all but 3% match within 4σ . This is different from a Gaussian error distribution, possibly indicating underestimated uncertainties in either published values or our own astrometric solution. The mean difference between μ_{α} and μ_{δ} values was 4 ± 32 mas and -4 ± 30 mas, respectively. No systematic trends were detected in the proper motion component differences. We list objects whose μ_{α} or μ_{δ} components were discrepant by more than 4σ in Table 4. 2M1404-3159 is among the discrepant proper motion objects yet we believe there was a sign reporting error in Looper et al. (2007) as we calculate the same magnitude of motion in the opposite direction.

4. ABSOLUTE MAGNITUDE RELATIONS

As of 2011 September there were 106 L and T dwarfs with published parallax measurements. We have added 59 to this list, doubling the number of measurements in some spectral bins. The precision on parallaxes in this work as well as within the literature varies greatly. To ensure that the analysis that follows was not biased by uncertain parallaxes or photometry, we required all sources to have M_{JHK} uncertainty < 0.5 mag. We list photometry, parallax measurements, and references for all known and new UCDs in Table 5. With a substantial increase in the number of objects, we can re-evaluate the color–magnitude and spectral type luminosity trends originally defined by Dahn et al. (2002), Tinney et al. (2003), and Vrba et al. (2004), particularly across the poorly sampled L/T transition region. We list all L and T dwarfs with parallaxes and their corresponding

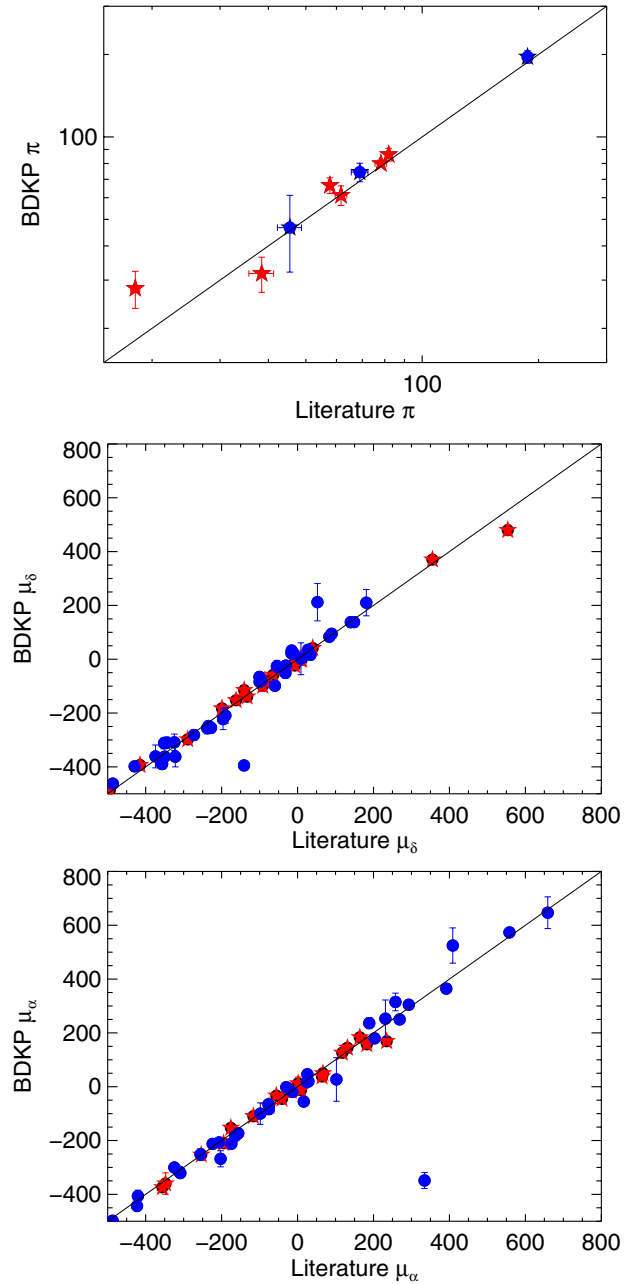


Figure 2. Top plot: the parallax measurement comparison of the nine calibrator dwarfs. All but two match previous measurements within 1σ . Middle and lower plots: comparison of literature proper motion components to those measured in this work. Three objects are discrepant by more than 4σ and listed in Table 4. In each plot blue filled circles represent dwarfs that were measured with ISPI and red five point stars were measured with ANDICAM.

(A color version of this figure is available in the online journal.)

Table 3
Astrometric Calibrators

Name	π_{abs} (mas) (BDKP)	μ_{α} (mas yr ⁻¹) (BDKP)	μ_{δ} (mas yr ⁻¹) (BDKP)	π_{abs} (mas) (Lit)	μ_{α} (mas yr ⁻¹) (Lit)	μ_{δ} (mas yr ⁻¹) (Lit)	Inst. ^a	Ref
(1)	(2)	(3)	(4)	(5)	(6)	(7)	(8)	(9)
LHS 1777	79.9 ± 2.5	-175.6 ± 2.2	937.9 ± 2.3	78.20 ± 2.70 79.72 ± 1.89 80.11 ± 2.34	-153.00 ± 5.00	957.00 ± 5.00	A	1 2 3
WT 248	31.7 ± 4.7	-1199.4 ± 5.9	-140.5 ± 5.8	38.44 ± 2.83	-1191.00 ± 13.00	-115.00 ± 13.00	A	1
2MASS J0746+2000	86.2 ± 4.6	-355.9 ± 5.1	-63.7 ± 5.2	81.90 ± 0.30	-374.04 ± 0.31	-57.91 ± 0.65	A	4
2MASS J0939-2448	196.0 ± 10.4	558.1 ± 5.8	-1030.5 ± 5.6	187.30 ± 4.60	573.40 ± 2.30	-1044.70 ± 2.50	I	6
TWA28	28.0 ± 4.3	-55.7 ± 3.9	-7.4 ± 3.8	18.1 ± 0.5	-67.2 ± 0.6	-14.0 ± 0.6	A	8
2MASS J1058-1548	66.5 ± 4.4	-253.5 ± 3.4	39.7 ± 3.2	57.70 ± 1.00	-252.93 ± 0.50	41.42 ± 0.45	A	4
2MASS J1444-2019	61.2 ± 5.1	-2905.1 ± 3.4	-1953.9 ± 3.4	61.67 ± 2.12	-2906.15 ± 2.41	-1963.12 ± 2.71	A	7
SDSS J1446+0024	46.7 ± 14.6	202.9 ± 10.9	-100.4 ± 10.8	45.46 ± 3.25	179.60 ± 6.68	-65.58 ± 4.07	I	5
2MASS J2356-1553	74.4 ± 5.8	-422.7 ± 4.0	-615.9 ± 3.6	68.97 ± 3.42	-443.44 ± 2.07	-600.15 ± 2.48	I	5

Notes. ^a A: ANDICAM and I: ISPI.

References. (1) van Altena et al. 1995; (2) Jao et al. 2005; (3) Costa et al. 2005; (4) Dahn et al. 2002; (5) Vrba et al. 2004; (6) Burgasser et al. 2008c; (7) Schilbach et al. 2009; (8) Teixeira et al. 2008.

Table 4
Discrepant Proper Motion Values

Name	μ_{α} (mas yr ⁻¹) (BDKP)	μ_{δ} (mas yr ⁻¹) (BDKP)	μ_{α} (mas yr ⁻¹) (Lit)	μ_{δ} (mas yr ⁻¹) (Lit)	Reference
2MASSJ06164006-6407194	1304.0 ± 3.9	-31.9 ± 3.7	1405 ± 8	-51 ± 18	1
2MASSJ14044941-3159329 ^a	334.5 ± 4.9	-15.5 ± 4.7	-348 ± 30	32 ± 3	2
2MASSJ21321145+1341584	16.4 ± 11.6	-141.0 ± 11.2	-55 ± 9	-395 ± 9	3

Notes. Details on the discrepant proper motion objects. We note only objects whose proper motion values were discrepant by more than 4σ .

^a We find the same magnitude of motion as Looper et al. (2007) yet an opposite direction. We conclude there must be a sign error in that work.

References. (1) Cushing et al. 2009; (2) Looper et al. 2007; (3) Siegler et al. 2007.

magnitudes in optical through mid-IR wavelengths in Table 5. The apparent MKO JHK magnitudes listed in Table 5 were used to calculate the absolute MKO M_{JHK} magnitudes used throughout the analysis.

Figure 3 shows the M_{JHK} magnitude versus spectral type for all late-type M, L, and T dwarfs with parallax measurements. Seemingly normal field objects (hereafter “normal” is defined as excluding tight binaries unresolved in 2MASS, young sources with low surface gravity features, and subdwarfs) provide a guideline for how near-IR intrinsic brightness changes with spectral type. Absolute magnitudes of brown dwarf subgroups (unresolved binaries in red, subdwarfs in blue, and low surface gravity or companions to young field stars in green and purple) allow us to investigate how secondary parameters such as binarity, metallicity, and age influence brown dwarf observables. In this section, we investigate what can be extrapolated for the population using the sequence of normal field dwarfs including resolved L/T transition binaries. In Sections 6, 7, and 9 we discuss in detail the differences among the subdwarfs, low surface gravity, and binary dwarfs, respectively.

Brown dwarfs have highly structured spectral energy distributions, and magnitudes in JHK are extremely sensitive to the exact filter bandpass used. Therefore, we converted all magnitudes onto the Mauna Kea Observatory filter set (MKO; Tokunaga et al. 2002), whose narrow bandpasses are less affected by atmospheric absorption than the CIT and 2MASS fil-

ter sets (particularly at J). If required, the transformations from Stephens & Leggett (2004) were used to convert from 2MASS to MKO magnitudes.

Most of the L dwarfs in our sample were classified spectrally from red optical data following the scheme of Kirkpatrick et al. (1999), while the T dwarfs were classified in the near-IR (Burgasser et al. 2006a). An optical spectral type was used for any object classified as an L dwarf and a near-IR spectral type was used for any object classified as a T dwarf. For any L dwarf lacking optical data we used its near-IR spectral type.

4.1. Brown Dwarf H-R Diagram

Figure 4 shows the M_{JHK} sequence for normal L and T dwarfs with uncertainties <0.5 mag. We have distinguished published parallaxes (open circles) from those reported in this work (filled gray circles) to demonstrate the impact of these new measurements. We have augmented the field dwarf sample in Figure 5 with resolved photometry for 9 L-dwarf/T-dwarf transition binaries for a more detailed look at brightness trends across this transition (Burgasser et al. 2010a; Looper et al. 2008a; McCaughrean et al. 2004; Liu et al. 2010; Stumpf et al. 2011). Four known binary sources, 2MASS J0518-2828, 2MASS J1209-1004, 2MASS J1404-3159, and SDSS J2052-1609 had parallax measurements reported in this work as did one suspected binary SDSS J1511+0607 (Burgasser et al. 2010a; C. R. Gelino et al. in preparation). We list the

Table 5
Photometry of Full Sample^a

Name	SpT (OpT)	SpT (near-IR)	π (mas)	J (MKO)	H (MKO)	K (MKO)	Note ^b	Ref
(1)	(2)	(3)	(4)	(5)	(6)	(7)	(8)	(9)
2MASSJ00043484–4044058	L5.0	L4.5	76.86 ± 3.97	13.06 ± 0.03	12.14 ± 0.03	11.36 ± 0.03	B	23, 65, 9, 70
2MASSJ00250365+4759191	L4.0	–	23.69 ± 1.08	14.72 ± 0.04	13.71 ± 0.03	12.85 ± 0.06	B	13, 94
2MASSJ00303013–1450333	L7.0	–	37.42 ± 4.50	16.39 ± 0.03	15.37 ± 0.03	14.49 ± 0.03	N	15, 74
2MASSJ00325584–4405058	L0.0 γ	–	38.42 ± 4.80	14.68 ± 0.04	13.89 ± 0.03	13.23 ± 0.04	LG	1, 23, 22
2MASSJ00325937+1410371	–	L8.0	30.14 ± 5.16	16.58 ± 0.05	15.66 ± 0.05	14.99 ± 0.05	N	34, 74
ULASJ00340277–0052067	–	T8.5	79.60 ± 3.80	18.15 ± 0.04	18.49 ± 0.04	18.48 ± 0.04	N	59
2MASSJ00345157+0523050	–	T6.5	105.36 ± 7.48	15.11 ± 0.03	15.55 ± 0.03	15.96 ± 0.03	N	1, 24, 19
2MASSJ00361617+1821104	L3.5	L4.0	114.20 ± 0.80	12.30 ± 0.03	11.64 ± 0.03	11.04 ± 0.03	N	10, 15, 9, 69
HD3651B	–	T7.5	90.03 ± 0.72	16.31 ± 0.03	16.72 ± 0.03	16.86 ± 0.03	N	54, 46, 71
CFBDSJ00591090–0114013	–	T9.0	108.20 ± 5.00	18.06 ± 0.05	18.27 ± 0.05	18.71 ± 0.05	N	60

Notes. Table contains all sources with parallaxes reported in this work as well as all sources used in the astrometric analysis (with absolute magnitude uncertainty <0.5 mag).

^a See the online version for the full table containing *rizYJHKLM* and IRAC [3.6,4.5,5.8,8.0] bands where available.

^b LG is a low surface gravity dwarf, Cal is a calibrator ultracool dwarf, SD is an ultracool subdwarf, and B is a tight binary unresolved in 2MASS.

^c Objects PS043, ULAS1416, SOSS J1416, and CFBOS 1458AB were added during the proof process and not used in the analysis throughout the paper.

References. (1) This paper; (2) Chiu et al. 2006; (3) Cruz et al. 2003; (4) Gizis et al. 2000; (5) Golimowski et al. 2004; (6) Hawley et al. 2002; (7) Kendall et al. 2004; (8) Kirkpatrick et al. 1997; (9) Knapp et al. 2004; (10) Reid et al. 2000; (11) Ruiz et al. 1997; (12) Wilson et al. 2001; (13) Cruz et al. 2007; (14) Kirkpatrick et al. 1999; (15) Kirkpatrick et al. 2000; (16) Kirkpatrick et al. 2008; (17) Reid et al. 2008; (18) Forveille et al. 2004; (19) Burgasser et al. 2006a; (20) Burgasser et al. 2008a; (21) Stumpf et al. 2008; (22) Cruz et al. 2009; (23) EROS Collaboration et al. 1999; (24) Burgasser et al. 2003d; (25) Looper et al. 2007; (26) Burgasser et al. 2004; (27) Cruz et al. 2004; (28) Burgasser et al. 2000b; (29) Burgasser et al. 2003b; (30) Cushing et al. 2009; (31) Tinney et al. 2005; (32) Burgasser et al. 2002a; (33) Delfosse et al. 1997; (34) Geballe et al. 2002; (35) Looper et al. 2008a; (36) Burgasser et al. 2002a; (37) Lépine et al. 2003a; (38) Ellis et al. 2005; (39) Martin et al. 1999; (40) Thorstensen & Kirkpatrick 2003; (41) Burgasser et al. 2004; (42) Fan et al. 2000; (43) Burgasser et al. 2003a; (44) Scholz et al. 2003; (45) Leggett et al. 2000; (46) Luhman et al. 2007; (47) Lodieu et al. 2007; (48) Biller et al. 2006; (49) Strauss et al. 1999; (50) Burgasser et al. 1999; (51) Artigau et al. 2010; (52) Tsvetanov et al. 2000; (53) Nakajima et al. 1995; (54) Mugrauer et al. 2006; (55) Pinfield et al. 2008; (56) Burgasser et al. 2000a; (57) Goldman et al. 2010; (58) Burningham et al. 2009; (59) Warren et al. 2007; (60) Delorme et al. 2008; (61) Burningham et al. 2008; (62) Lucas et al. 2010; (63) Schneider et al. 2002; (64) Burgasser et al. 2007; (65) Kirkpatrick et al. 2001; (66) Kasper et al. 2007; (67) Burgasser et al. 2010b; (68) Costa et al. 2006; (69) Dahn et al. 2002; (70) Henry et al. 2006; (71) Perryman et al. 1997; (72) Schilbach et al. 2009; (73) Tinney et al. 2003; (74) Vrba et al. 2004; (75) Harrington & Dahn 1980; (76) Reid & Cruz 2002; (77) Phan-Bao et al. 2006; (78) Reid et al. 1995; (79) Rice et al. 2010; (80) Jao et al. 2005; (81) Cruz et al. 2009; (82) Scholz et al. 2004b; (83) Chauvin et al. 2005; (84) Faherty et al. 2011; (85) van Altena et al. 1995; (86) Monet et al. 1992; (87) Bowler et al. 2009; (88) van Leeuwen 2007; (89) Scholz et al. 2004a; (90) Scholz et al. 2004b; (91) Lépine et al. 2003a; (92) Lépine et al. 2003b; (93) Lépine et al. 2003c; (94) Faherty et al. 2010; (95) Becklin & Zuckerman 1988; (96) Andrei et al. 2011; (97) Metchev & Hillenbrand 2004; (98) Delfosse et al. 1999; (99) Sivarani et al. 2009; (100) Burgasser et al. 2009; (101) Potter et al. 2002; (102) Goto et al. 2002; (103) Metchev & Hillenbrand 2006; (104) Liu et al. (2011); (105) Scholz (2010); (106) Bowler et al. (2010); (107) Schmidt et al. (2010); (108) Liu et al. (2011); (109) Delorme et al. (2010).

(This table is available in its entirety in a machine-readable form in the online journal. A portion is shown here for guidance regarding its form and content.)

component magnitudes of the binaries (including all known binary L/T transition objects with parallaxes) in Table 6.

We have used the full parallax sample of normal objects with M_{JHK} uncertainties <0.5 mag to re-examine commonly used near-infrared absolute magnitude/spectral type relations. To determine the best fit between these parameters, we applied an F -test to a polynomial with increasing coefficients. The F -test allows us to distinguish the false-alarm probability of a decreasing χ^2 due to additional degrees of freedom. In this manner, we converged on a fourth-order fit to spectral type versus MKO M_{JHK} for normal field dwarfs. The coefficients are listed in Table 7 and the solution is overplotted in Figure 5. For comparison, Marocco et al. (2010) recently reported 11 mid- to late-type T dwarf parallaxes and also converged upon a fourth-order polynomial fit to MKO M_{JHK} for L0–T9 dwarfs. In that work, near-IR spectral types were used for L0–T9 likely leading to a steeper fit for L dwarfs than our fit. In the same manner as Liu et al. (2006), Marocco et al. (2010) report two absolute magnitude/spectral type polynomials (overplotted as red dashed lines in Figure 5): the first excluding known binaries and the second excluding known binaries as well as five binary candidates across the L/T transition (as selected by Liu et al.). Liu et al. (2006) found a 0.6 mag difference between the peak of the L/T transition when excluding binary candidates but with the addition of the Marocco et al. (2010) parallax sample this

was reduced to 0.2 mag. Adding our new parallaxes, we find no difference in a polynomial fit that excludes or does not exclude the five binary candidates, therefore we report one fit for the entire sample.

As the data indicate in Figure 5, the brightening across the L/T transition is more pronounced than demonstrated by a polynomial fit from L0 to T9. By eye, the L dwarfs, L/T transition objects and T dwarfs appear to follow distinct and independent linear trends. Therefore, as an alternative to a full range L0–T9 polynomial, we have split the normal, single source objects in Figure 4 into three ranges of L0–L9, T0–T4, and T5–T9 and fit a linear polynomial to each. We obtained uncertainties on the coefficients by randomly shifting the known objects in each range within the given uncertainty 10,000 times and fitting a Gaussian to the range of parameters. The best-fit piecewise lines are overplotted in Figure 4 and reported in Table 8. For the L/T transition between T0 and T4, we find a brightening at J between [1.2–1.4] mag, a brightening at H between [0.3–0.5] mag, and a plateau or dimming at K between [–0.2 to –0.3] mag. The increased sampling across the L/T transition demonstrates that the brightening is a real and prominent feature, however further investigation of individual objects is necessary to disentangle the role that dust and unresolved binarity play in creating the effect. We discuss the L/T transition objects in relation to model predictions in

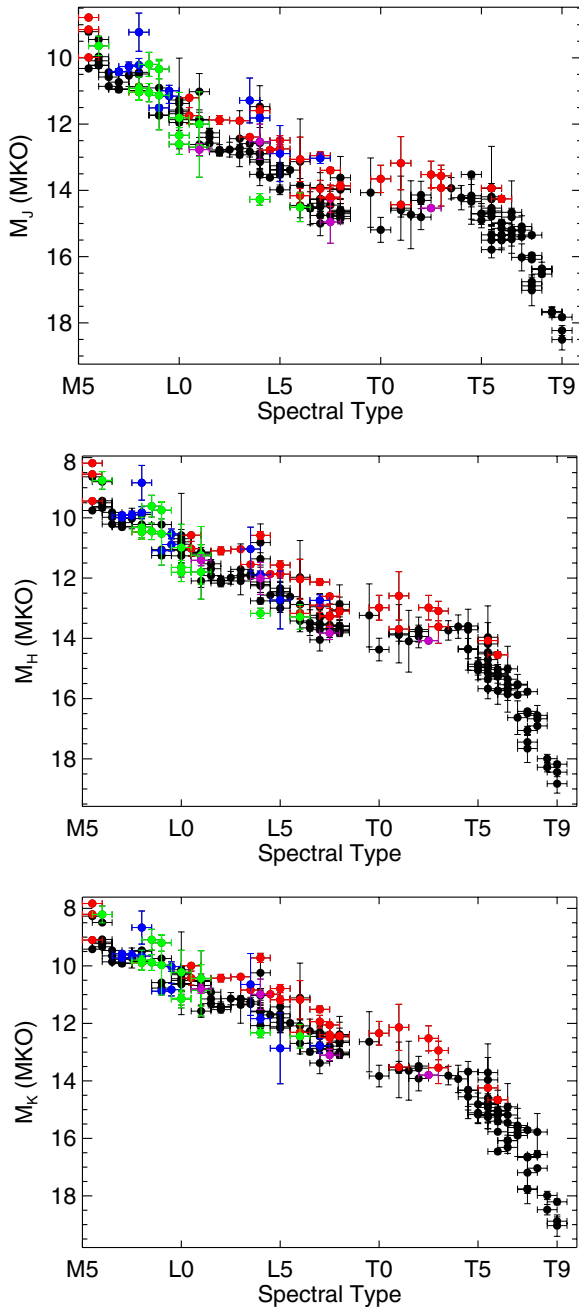


Figure 3. Spectral type vs. absolute magnitude in the MKO *JHK* filters for normal (black filled circles), combined-light binary (red filled circles), young (companions to known $\ll 1$ Gyr stars; purple filled circles), low surface gravity (green filled circles), and subdwarf (blue filled circles) M through T dwarfs. All UCDs with a parallax measurement in this work or within the literature are shown regardless of uncertainty.

(A color version of this figure is available in the online journal.)

Section 5.3. We have used the full parallax sample of the normal objects with M_{JHK} uncertainties ≤ 0.5 mag to re-examine commonly used near-infrared absolute magnitude/spectral type relations. Details on the full sample of objects used in our analysis as well as mean absolute magnitude values in M_{JHK} are shown in Table 9

4.2. Color–Magnitude Trends for L and T Dwarfs

We have collected photometric information (from optical to mid-IR) for all known L and T dwarfs with parallaxes

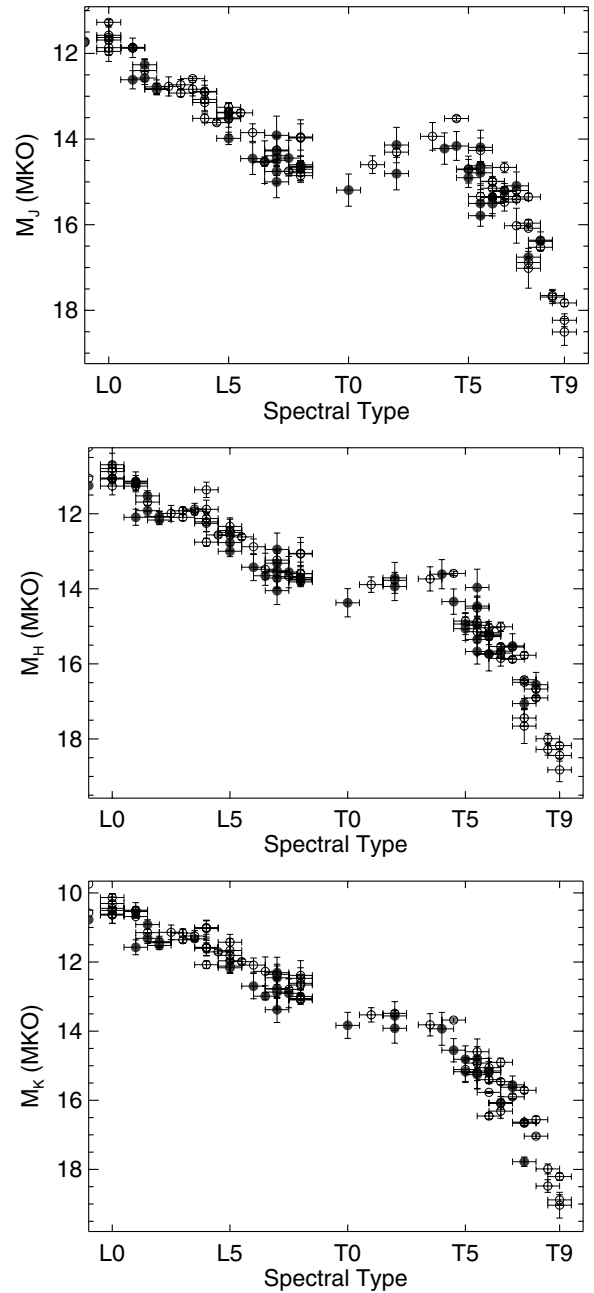


Figure 4. Spectral type vs. absolute magnitude in the MKO *JHK* filters for normal L through T dwarfs. Unfilled circles are ultracool dwarfs with parallax measurements gathered from the literature and filled circles are those reported in this work. Low surface gravity, subdwarf, binary, and young companion brown dwarfs are not shown. Only objects with absolute magnitude uncertainties < 0.5 mag are displayed.

(106 from the literature and 59 added in this work), totaling 165 (see Table 5). We examined various combinations of optical, near-IR, and mid-IR colors to find correlations on color–magnitude diagrams that provided the strongest insight into differentiating brown dwarf spectral types and/or physical properties of the population. Figures 6 and 7 show representative color–magnitude diagrams using only objects whose absolute magnitude uncertainties are < 0.5 mag.

Figure 6 shows the most striking linear relationship between color and absolute magnitude. Patten et al. (2006) first showed a relatively smooth progression of M through T dwarfs in the M_K versus $K_s - [4.5]$ diagram. We verify that this relation separates

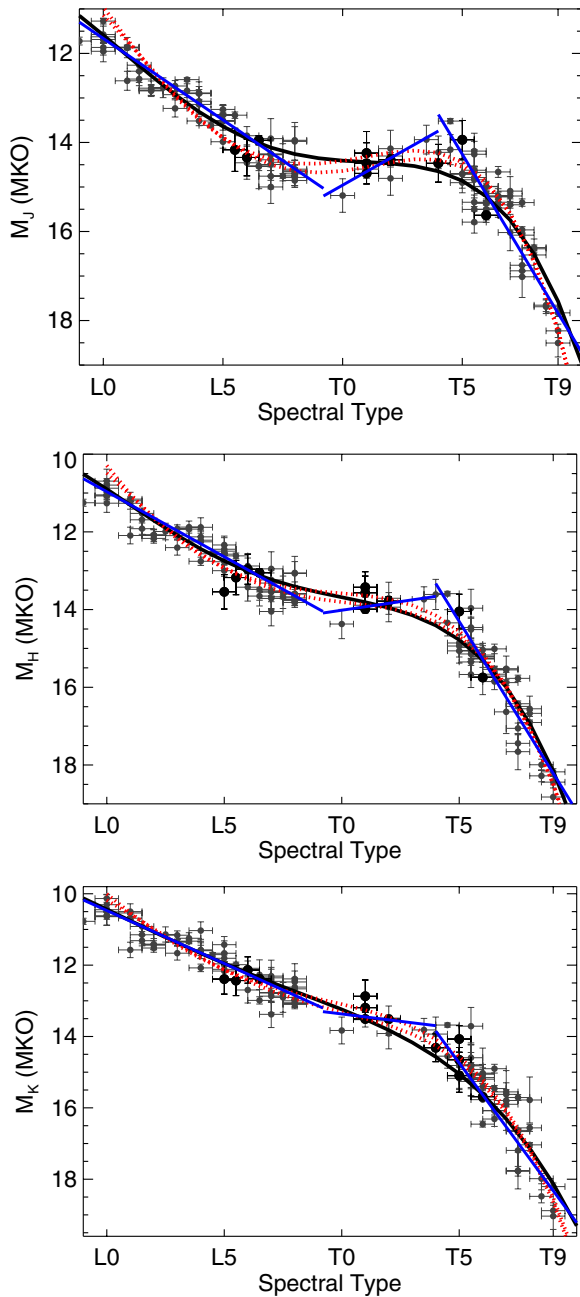


Figure 5. Spectral type vs. absolute magnitude in the MKO JHK filters for normal L and T dwarfs and L/T transition binaries with resolved components. Light gray filled circles represent normal field dwarfs. Black filled circles are the resolved absolute magnitudes of the binary components. Overplotted on each panel is the best-fit polynomial for L0–T9 dwarfs (see Table 7) in solid black, the bright/faint polynomials in red-dashed from Marocco et al. (2010), and the best-fit linear functions to the ranges L0–L9, T0–T4, and T5–T9 in solid blue. Only objects with absolute magnitude uncertainties <0.5 mag are shown.

(A color version of this figure is available in the online journal.)

the early and mid-L dwarfs ($0.5 < K-[4.5] < 1.4$) from the early and mid-T dwarfs ($1.4 < K-[4.5] < 4.0$). However, it does not show a linear progression with spectral subtypes. The degeneracy is most clearly depicted for the T6.0 and T6.5 dwarfs (designated by gray triangle symbols) which have a nearly 2.0 mag spread in $K-[4.5]$ color.

Interestingly the low surface gravity dwarfs, depicted as filled downward-facing triangles, appear slightly overluminous for their color in comparison to normal field dwarfs.

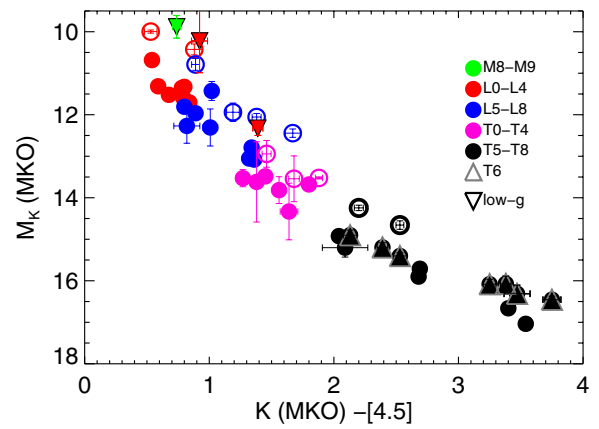


Figure 6. Tightest linear relationship between color and luminosity identified for brown dwarfs. L dwarfs smoothly transition into T dwarfs although the figure is nonlinear for spectral subtypes (as depicted by the T6 dwarfs in gray upward-facing triangles). Unresolved binaries are shown as open circles. Low surface gravity dwarfs are shown as downward-facing triangles and appear slightly overluminous for their color.

(A color version of this figure is available in the online journal.)

This is in contradiction to findings discussed in Section 6 where objects are underluminous in M_{JHK} for their spectral type. The discrepancy between the behavior of low gravity objects on the mid-IR color–magnitude diagram and the spectral-type/absolute magnitude diagrams suggests that spectral type is a poor gauge for effective temperature of young objects.

The most prevalent change on these color–magnitude diagrams is a color reversal. Figure 7 shows the three most studied versions of this effect. Condensate cloud opacity is likely the dominate contributor to the increasingly red colors of L dwarfs and the onset of CH_4 is responsible for the change to blue as temperatures drop into the T dwarf regime. As objects transition from L into T dwarfs the brightening (discussed in Section 4.1) is most clearly seen in the J band although it is seen to a lesser effect in H and plateaus in K . Subdwarfs occupy their own space on this diagram with extremely blue near-IR colors. Low surface gravity dwarfs fall within the color space of normal field dwarfs; however, they are redward and underluminous compared to normal dwarfs with the same spectral type. In Section 5 below, we discuss the M_K versus $J - K$ color–magnitude diagram in context against models to disentangle subtle effects that drive much of the scatter seen in Figure 7.

5. COMPARISON TO EVOLUTIONARY MODELS

To put the observed trends on color–magnitude diagrams in context, we compared the data to two sets of evolutionary models. Saumon & Marley (2008) present a set of models that include a cloud sedimentation parameter and three gravity choices ($\log(g) = [4.5, 5.0, 5.5]$) which can be varied to explain (with different levels of accuracy) the near-IR color–magnitude diagram for L and T dwarfs. Burrows et al. (2006) present a model that includes refractory clouds as well as a completely cloudless model with varying gravity and metallicity parameters. In Figures 8 and 9 we examine the M_K versus $J - K$ diagram for L and T dwarfs using the full sample with trigonometric parallaxes and the respective evolutionary models. In Figure 8, the sedimentation parameter (f_{sed}) from Saumon & Marley (2008) is shown with increasing value and varying gravity to represent decreasing cloud thickness. In Figure 9, metallicity and

Table 6
Magnitudes for L/T Transition Binaries

Name	SpT Combined	SpT Primary	SpT Secondary	M_J Primary	M_J Secondary	M_H Primary	M_H Secondary	M_K Primary	M_K Secondary	Ref
(1)	(2)	(3)	(4)	(5)	(6)	(7)	(8)	(9)	(10)	(11)
SD0423–0414	L7.5	L6.5	T2.0	13.95 ± 0.10	14.39 ± 0.12	13.05 ± 0.10	13.78 ± 0.12	12.38 ± 0.09	13.51 ± 0.06	1
2M0518–2828	L7.5	L6.0	T4.0	14.34 ± 0.41	14.47 ± 0.42	12.96 ± 0.39	14.29 ± 0.51	12.14 ± 0.37	14.32 ± 0.39	1
SD1021–0304	T3.0	T1.0	T5.0	14.24 ± 0.48	14.40 ± 0.51	13.42 ± 0.40	14.54 ± 0.57	13.19 ± 0.36	14.65 ± 0.35	1
2M1404–3159	T2.5	T1.0	T5.0	14.47 ± 0.46	13.94 ± 0.43	13.57 ± 0.43	14.05 ± 0.45	12.87 ± 0.45	14.07 ± 0.38	2
2M1711+2232	L6.5	L5.0	T5.5	15.08 ± 0.52	16.00 ± 0.59	13.54 ± 0.44	15.64 ± 0.75	12.39 ± 0.42	15.44 ± 0.65	1
SD1511+0607	T0.0	L5.5	T5.0	14.17 ± 0.48	14.72 ± 0.55	13.18 ± 0.44	14.96 ± 0.65	12.43 ± 0.42	15.09 ± 0.47	1
Epsilon Indi	T2.5	T1.0	T6.0	14.69 ± 0.04	15.63 ± 0.04	13.99 ± 0.04	15.75 ± 0.04	13.51 ± 0.04	15.69 ± 0.01	3
2M1209–1004	T3.0	T2.0	T7.5	14.17 ± 0.57	15.64 ± 0.69	13.69 ± 0.56	16.45 ± 0.78	13.59 ± 0.56	16.85 ± 1.04	4
2M2052–1609	T1.0	T1.0	T3.5	14.04 ± 0.92	14.19 ± 0.93	13.05 ± 0.89	13.61 ± 0.89	12.67 ± 0.92	13.42 ± 0.79	5

References. (1) Burgasser et al. 2010a; (2) Looper et al. 2008a; (3) McCaughrean et al. 2004; (4) Liu et al. 2010; (5) Stumpf et al. 2011.

Table 7
Coefficients of Polynomial Fits for L0–T8 Dwarfs

MKO Filter	c_0	c_1	c_2	c_3	c_4	rms
(1)	(2)	(3)	(4)	(5)	(6)	(7)
M_J^a	1.48948e+1	−1.99967e+0	2.75734e−1	−1.29143e−2	2.03252e−4	0.30
M_H^a	1.32372e+1	−1.60036e+0	2.27363e−1	−1.08205e−2	1.75368e−4	0.27
M_K^a	9.76100e+0	−4.85519e−1	9.40816e−2	−4.69032e−3	8.16516e−5	0.28

Notes. Relations use (MKO) magnitudes. Polynomial fits to optical L dwarfs and NIR T dwarfs (L dwarfs with no optical spectral type have NIR spectral types) excluding subdwarfs, low gravity dwarfs, and binaries. Function is defined as $M_{J,H,K} = \sum_{i=0}^n c_i(\text{SpT})^i$ and is valid for spectral types L0–T8 where 10 = L0, 20 = T0, etc.

^a Including 8 L/T transition binaries with resolved photometry: SDSS J0423–0414, 2MASS J0518–2828, SDSS J1021–0304, 2MASS J1404–3159, 2MASS J1711+2232, SDSS J1511+0607, Epsilon Indi, SDSS J1534+1615.

Table 8
Coefficients of Piecewise Fits for L0–T9 Dwarfs

MKO Filter	c_0	c_1	SpT range
(1)	(2)	(3)	
M_J	0.366 ± 0.002	8.003 ± 0.025	L0–L9
M_H	0.335 ± 0.002	7.616 ± 0.025	
M_K	0.297 ± 0.002	7.500 ± 0.025	
M_J	$−0.304 \pm 0.020$	21.039 ± 0.438	T0–T4.0
M_H	$−0.089 \pm 0.020$	15.797 ± 0.432	
M_K	0.082 ± 0.019	11.729 ± 0.430	
M_J	0.892 ± 0.008	$−8.035 \pm 0.212$	T5.0–T9.0
M_H	0.977 ± 0.008	$−10.119 \pm 0.225$	
M_K	0.895 ± 0.006	$−7.632 \pm 0.163$	

Note. See Table 7 comments.

gravity variations are examined using the models of Burrows et al. (2006). All early and late-type L and T dwarfs (including subdwarfs) with trigonometric parallaxes ($\sigma_{M_K} < 0.5$ mag) are overplotted. In the following subsections, we discuss how variations of the models fit different spectral types. The low surface gravity dwarfs are discussed in detail in Section 6.

5.1. L Dwarfs

Varying gravity and metallicity within the cloud model of Burrows et al. (2006) encompasses the majority of early L dwarfs (top right and bottom two panels of Figure 9); however, late-type L dwarfs are still poorly represented. Compared to the highest gravity, super solar metallicity track, there are a number of late-type L dwarfs that are fainter and redward of predictions. In Figure 8, the L dwarf sequence is best modeled with the $f_{\text{sed}} = 1, 2$ parameters (top right and bottom left plots

of Figure 8). However, there are a handful of red or potentially “ultra-cloudy” objects that are not fit by either model. Significant outliers include 2MASS J1442+6603, which is a close (~ 30 AU) companion to the moderately young M1.5 dwarf G239–25 (Forveille et al. 2004), and 2MASS J0619–5803 which is a companion (~ 260 AU) to the young K2 star AB Pic (Chauvin et al. 2005). The independent assessment that these objects are young (or moderately young) yet redward of the cloudy model implies a connection between a youth and a dusty photosphere (further discussed in Section 6).

5.2. T Dwarfs

The mid- to late-type T dwarfs are best fit by the thin clouds ($f_{\text{sed}} = 4$) track from Saumon & Marley (2008) and the clear model from Burrows et al. (2006). In the case of the latter model (bottom right panel of Figure 8) the predicted range in both M_K and $J - K$ shows very little spread whereas empirical measurements show significant scatter. There are a handful of T dwarfs including those reported in this work, 2MASS J1114–2618, and 2MASS J1754+1649, as well as previously reported ULAS J0034–0052, ULAS J1335+1130, CFBDS J0059–0114, ULAS J0722–0540, and ROSS 458C which are notably underluminous and red compared to the $f_{\text{sed}} = 4$ model predictions. The colors of these late-type T dwarfs are better (or equally) fit by the $f_{\text{sed}} = 2$ parameter (thicker clouds) which also encompasses the majority of mid- to late-type L dwarfs. Comparing the spread to the Burrows et al. (2006) clear model (top left panel of Figure 9) shows similar red, underluminous outliers. Inconsistencies with both models suggest that thick condensate clouds continue to play a role in the photospheres of some cooler dwarfs (see discussion in Burgasser et al. 2010b; Marley et al. 2010). At least one of the

Table 9
Absolute Magnitudes With Resolved L/T Binaries

SpT	BDKP	Lit	Total	Norm	Bin	LG,Y	SD	M_J (MKO)	M_H (MKO)	M_K (MKO)
(1)	(2)	(3)	(4)	(5)	(6)	(7)	(8)	(9)	(10)	(11)
M6	1	8	9	8	0	1	0	10.23 ± 0.43	9.67 ± 0.42	9.33 ± 0.41
M7	0	7	7	4	0	0	3	10.93 ± 0.20	10.28 ± 0.13	9.90 ± 0.09
M8	4	5	9	4	0	4	1	10.87 ± 0.27	10.22 ± 0.24	9.84 ± 0.22
M9	2	5	7	3	0	1	3	11.72 ± 0.48	11.06 ± 0.55	10.58 ± 0.55
L0	2	8	10	6	2	2	0	11.69 ± 0.24	11.05 ± 0.21	10.51 ± 0.19
L1	3	5	8	7	0	1	0	12.26 ± 0.34	11.52 ± 0.37	10.92 ± 0.41
L2	3	2	5	4	1	0	0	12.82 ± 0.03	12.09 ± 0.07	11.44 ± 0.16
L3	0	6	6	4	2	0	0	12.84 ± 0.15	11.93 ± 0.10	11.33 ± 0.09
L4	1	9	10	6	2	1	1	13.15 ± 0.31	12.26 ± 0.31	11.60 ± 0.34
L5	3	7	10	8	2	0	0	13.51 ± 0.25	12.62 ± 0.22	11.99 ± 0.26
L6	4	4	8	6	1	1	0	14.52 ± 0.34	13.42 ± 0.29	12.47 ± 0.32
L7	8	7	15	9	5	0	1	14.44 ± 0.32	13.55 ± 0.31	12.78 ± 0.33
L8	0	9	9	8	1	0	0	14.66 ± 0.35	13.70 ± 0.31	13.00 ± 0.29
T0	2	0	2	1	1	0	0	—	—	—
T1	2	4	6	5	1	0	0	14.24 ± 0.29	13.42 ± 0.41	13.19 ± 0.47
T2	4	3	7	5	1	1	0	14.30 ± 0.37	13.77 ± 0.23	13.51 ± 0.25
T3	1	2	3	2	1	0	0	14.19 ± 0.18	13.74 ± 0.10	13.82 ± 0.28
T4	3	1	4	4	0	0	0	14.22 ± 0.52	14.34 ± 0.52	14.55 ± 0.47
T5	9	5	14	13	1	0	0	14.70 ± 0.58	14.89 ± 0.53	14.82 ± 0.51
T6	3	11	14	13	1	0	0	15.34 ± 0.27	15.54 ± 0.30	15.46 ± 0.52
T7	2	8	10	10	0	0	0	16.02 ± 0.72	16.49 ± 0.77	16.63 ± 0.87
T8	1	4	5	5	0	0	0	16.53 ± 0.69	16.91 ± 0.80	17.04 ± 1.08
T9	0	3	3	3	0	0	0	18.23 ± 0.34	18.44 ± 0.33	18.88 ± 0.44

Notes. All objects with parallaxes and absolute mag uncertainty <0.5 . Note that Bin are binaries, SD are subdwarfs, LG are low surface gravity dwarfs, and Y are young low mass companions.

ultra-cloudy T dwarf outliers, Ross 458C, is known to be young (Burgasser et al. 2010b; Burningham et al. 2011). A connection between youth and dust in the photospheres of T dwarfs is consistent with the L dwarf results discussed in Sections 5.1 and 6 of this work as well as recent modeling work of young exoplanets (Barman et al. 2011; Currie et al. 2011).

5.3. L/T Transition Dwarfs

The L/T transition objects are not fit by a single f_{sed} parameter using the Saumon & Marley (2008) models nor by any single combination of gravity and/or metallicity on the Burrows et al. (2006) models.¹⁶ The steady and significant decrease in $J-K$ color with near constant M_K for the objects in the transition region has been attributed to the clearing of clouds or a change in the atmospheric dynamical state (e.g., overall cloud thickness) as temperatures cool into the T dwarfs (see Burgasser et al. 2002b; Golimowski et al. 2004; Knapp et al. 2004). Without clouds to provide a significant, nearly gray opacity, flux can emerge through molecular opacity windows in J and H bands explaining the significant brightening discussed in Section 4.1.

To investigate whether our expanded parallax sample supports a rapid cloud clearing, we created a hybrid model using the Saumon & Marley tracks. Similar to the work of Burgasser et al. (2002b) we varied the sedimentation parameter between the $f_{\text{sed}} = 2$ and $f_{\text{sed}} = 4$ models across the region between $13.0 < M_K < 15.0$. We started with the $f_{\text{sed}} = 2$ color, then added the $f_{\text{sed}} = 4$ color in 10% increments across the transition. The result is plotted in Figure 10. The L/T transition objects lie within an

absolute magnitude range corresponding to model temperatures spanning ± 150 K from a mean T_{eff} that depends on the gravity chosen.

For an intermediate surface gravity of $\log(g) = 5.0$, which is consistent with field age objects (~ 3 Gyr), the mean T_{eff} of our model is $\sim 1200 \pm 100$ K for T0–T4 dwarfs. Golimowski et al. (2004) empirically measured the T_{eff} of 11 L7–T4 dwarfs and reported a near constant T_{eff} of ~ 1450 K. This warmer constant temperature across a broader range of spectral types was strong evidence for unresolved binarity across the transition. Indeed, 2 of the 11 objects in that sample have since been resolved into near-equal mass binaries. The splitting of spectral-type/absolute magnitude polynomials into bright and faint samples (see Section 4.1) was largely driven by this result. However, our result is in agreement with the outcome of other toy and sophisticated models (e.g., Burgasser et al. 2002b; Saumon & Marley 2008; Marley et al. 2010) which converged upon a similar cooler T_{eff} . Our comparatively lower temperature than found by Golimowski et al. (2004) across the transition is consistent with our finding that the brown dwarf temperature plateau occurs across a narrower spectral subtype range (T0–T4 rather than L7–T4) than previously thought.

6. LOW SURFACE GRAVITY DWARFS

A subset of our parallax sample are the low surface gravity dwarfs including seven M and seven L dwarfs. Their optical spectra are characterized by unusually weak FeH absorption, weak Na I and K I doublets, and very strong vanadium oxide bands (Cruz et al. 2009; Kirkpatrick et al. 2006). They have extreme red near-IR colors and small tangential velocities relative to the rest of the brown dwarf population (Faherty et al. 2009). Kirkpatrick et al. (2006) and Cruz et al. (2009) have

¹⁶ Burrows et al. (2006) also note that variations in cloud particle size cannot account for the transition objects.

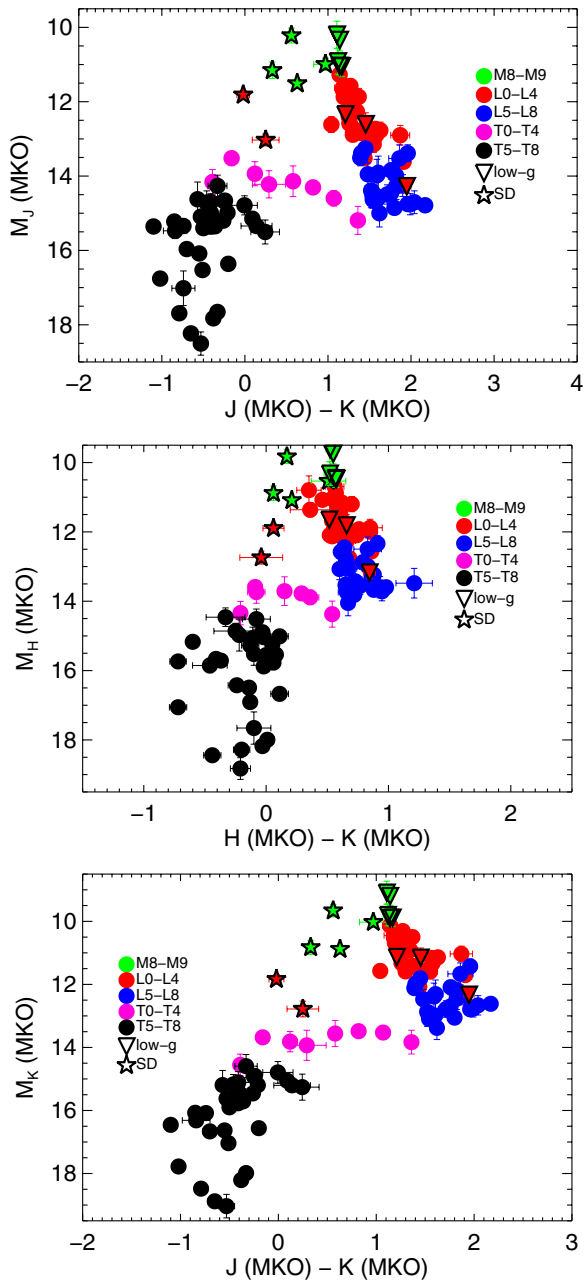


Figure 7. Near-IR color vs. absolute magnitude diagrams in a combination of MKO *JHK* filters. Spectral subtypes are color-coded and low-gravity as well as subdwarfs are depicted as downward-facing triangles and five point stars, respectively.

(A color version of this figure is available in the online journal.)

suggested that a number of the low surface gravity dwarfs are candidate members of nearby moving groups such as β Pictoris, Tucana-Horlogium, and AB Doradus, implying ages roughly spanning 10–50 Myr (e.g., Rice et al. 2010).

Younger UCDs have been examined on color–magnitude diagrams, but as only a handful have reported parallaxes, reports of under- or over luminosity have been speculative and in some cases contradictory. There is evidence that young dwarfs at the L/T transition such as HD 203030B and HN Peg B are underluminous or have a lower T_{eff} than equivalent spectral type dwarfs. This has been explained as a gravity dependent temperature/spectral type relation at the transition (Luhman et al. 2007; Metchev & Hillenbrand 2006). HR 8799b as well as

the early L dwarf companion to AB Pic are also underluminous while some earlier L and M dwarfs such as HD 130948B and CD-35 2722 B are overluminous on color–magnitude diagrams (Bowler et al. 2010; Chauvin et al. 2005; Dupuy et al. 2008; Wahhaj et al. 2011).

Figure 11 shows the near-IR absolute magnitude versus spectral type diagrams for normal mid-type M through late-type L dwarfs with the low surface gravity dwarfs and young companions overplotted. Table 10 lists the absolute magnitude for each object in *JHK* as well as the deviation from the M_{JHK} values for each spectral bin calculated from the polynomial in Table 7. Of the seven M dwarfs in this sample, three are >0.5 mag overluminous for their spectral type as might be expected for a young object which has not contracted to its final radius. Indeed, two of the three overluminous M dwarfs are suspected members of the TW Hydrae association. However, eight out of the ten low gravity or young companion L dwarfs ($\sim 80\%$) are $[0.2\text{--}1.0]$ mag underluminous for the average of their spectral subtype (compared to the polynomial described in Table 7) in one or more near-IR bands. In Figure 11, we have plotted the β and γ designations assigned for each object to indicate intermediate and low gravity, respectively (see the discussion in Kirkpatrick 2005; Cruz et al. 2009). Within this sample, there does not appear to be a correlation between ΔM_{JHK} (defined as the difference in M_{JHK} between the source and the predicted polynomial value) and the strength of low surface gravity features.

The trend of low surface gravity UCDs appearing underluminous for their spectral type is surprising given that young M dwarfs, such as those in TW Hydrae, are 1–2 mag overluminous (D. L. Looper et al. in preparation). While we find that the TW Hydrae M dwarfs in our sample are indeed overluminous, the L dwarfs show a different trend. According to the evolutionary tracks of Burrows et al. (1997), 10 Myr objects with masses ranging from 10 to 75 M_{Jup} have radii that are 25%–75% larger than 1–3 Gyr dwarfs with equivalent temperatures. This translates into an over luminosity of 0.5–1.2 mag. For 50 Myr objects radii can be 13%–50% larger and would be 0.3–0.9 mag overluminous. We speculate that there are at least two factors that could contribute to the underluminosity: first, the low-gravity spectral classification scheme may have a different temperature relation than the Kirkpatrick et al. (1999) classification scheme used for normal field dwarfs. For example, an L0 γ dwarf might have a significantly different temperature (and luminosity) than a normal L0 dwarf. Second, young objects could have dustier photospheres than field-aged dwarfs thus making young objects appear both fainter and redder than field objects of similar temperature. Observationally, both low surface gravity dwarfs and dusty L dwarfs show red near-IR colors and similar spectral characteristics (Looper et al. 2008b; Allers et al. 2010). Evolutionary models demonstrate that the lower gravity and dustier (lower f_{sed}) tracks have redder near-IR colors than intermediate, high gravity, or larger f_{sed} tracks (see Figure 12).

In Figure 12, we isolate the low surface gravity L dwarfs with M_K uncertainties <0.5 mag on a color–magnitude diagram with the Saumon & Marley (2008) and Burrows et al. (2006) evolutionary tracks overplotted. In general the sources do not follow the low-gravity track. Moreover, each model traces objects at temperatures that are several hundred degrees lower than expected for equivalent spectral type objects. For example, temperatures for L4 dwarfs range from ~ 1600 to 1900 K (Golimowski et al. 2004); however, the L4 γ dwarf, 2MASS J0501–0010, is traced by model temperatures of ~ 1200 –1300 K.

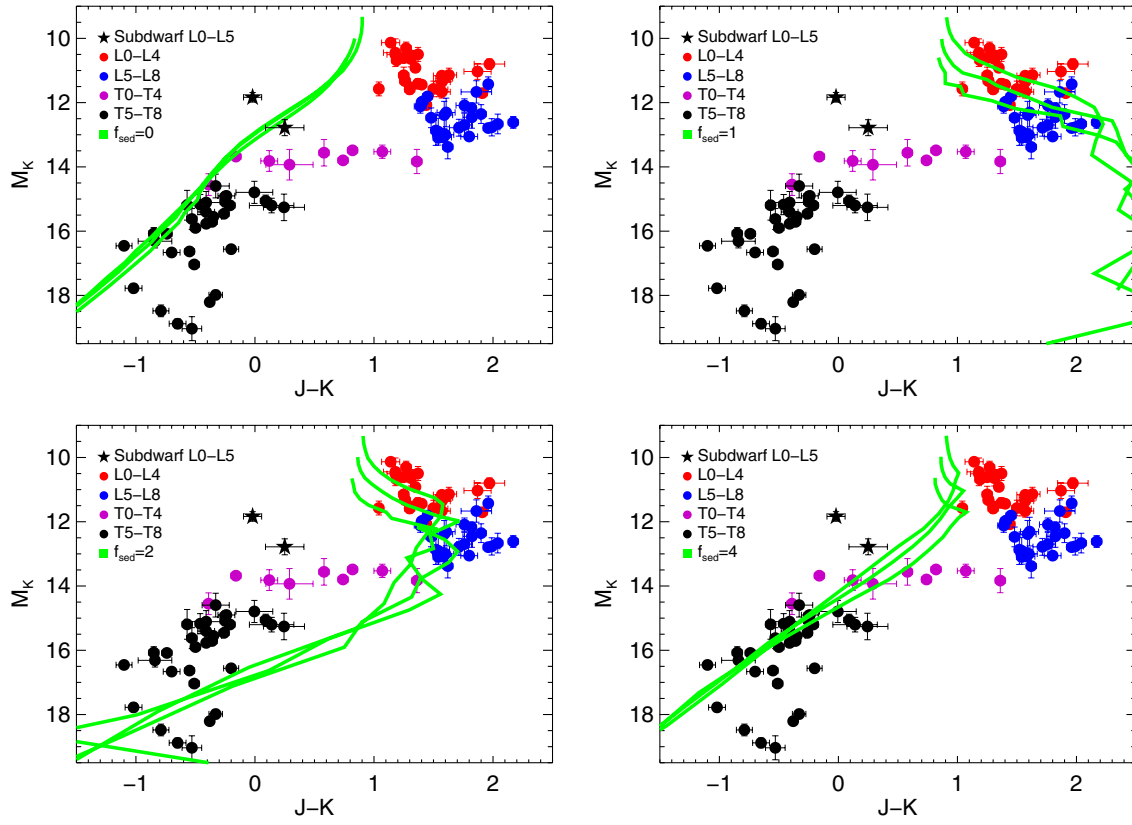


Figure 8. $J - K$ vs. M_K diagrams for L and T dwarfs with the evolutionary models of Saumon & Marley (2008) overplotted. Varying the cloud thickness parameter, f_{sed} , from thick ($f_{\text{sed}} = 1$) to thin ($f_{\text{sed}} = 4$) to cloudless (denoted as $f_{\text{sed}} = 0$), fits the L and T dwarf sequences with varying degrees of accuracy. The three different tracks in each plot represent different gravities ($\log(g) = [4.5, 5.0, 5.5]$).

(A color version of this figure is available in the online journal.)

Table 10
Low Gravity Dwarfs

Name (1)	Spt (2)	M_J (3)	M_H (4)	M_K (5)	$\Delta_{M_J}^a$ (6)	$\Delta_{M_H}^a$ (7)	$\Delta_{M_K}^a$ (8)
2MASS J0422+1530	M6 γ	9.6 ± 0.3	8.8 ± 0.3	8.2 ± 0.3	0.7	1.0	1.1
2MASS J0221-6831	M8 β	10.9 ± 0.3	10.3 ± 0.3	9.8 ± 0.3	-0.2	-0.2	0.0
2MASS J0652-5741	M8 β	11.0 ± 0.3	10.5 ± 0.2	9.9 ± 0.2	-0.3	-0.3	-0.1
2MASS J0608-2753 ^b	M8.5 γ	11.1 ± 0.3	10.5 ± 0.3	9.9 ± 0.3	-0.1	-0.1	0.1
TWA28	M8.5 γ	10.2 ± 0.4	9.6 ± 0.4	9.1 ± 0.4	0.8	0.7	0.9
2MASS J1022+0200	M9 β	11.1 ± 1.0	10.5 ± 1.0	10.0 ± 1.0	0.0	0.0	0.2
TWA 26	M9 γ	10.3 ± 0.3	9.8 ± 0.3	9.2 ± 0.3	0.8	0.8	0.9
2MASS J0518-2756	L0 γ	11.8 ± 0.8	11.0 ± 0.8	10.2 ± 0.8	-0.2	-0.1	0.2
2MASS J0032-4405	L0 γ	12.6 ± 0.3	11.8 ± 0.3	11.2 ± 0.3	-1.0	-0.9	-0.7
2MASS J2322-3133	L0 β	12.3 ± 0.2	11.7 ± 0.2	11.1 ± 0.2	-0.8	-0.8	-0.7
2MASS J0712-6155	L1 β	12.0 ± 1.0	11.2 ± 1.0	10.4 ± 1.0	0.1	0.1	0.3
2MASS J0536-1920	L1 β	12.7 ± 0.9	11.8 ± 0.9	10.9 ± 0.9	-0.6	-0.5	-0.1
AB Pic ^c	L1 ^c	12.8 ± 0.2	11.4 ± 0.2	10.8 ± 0.2	-0.7	-0.1	0.0
2MASS J0501-0010	L4 γ	14.3 ± 0.2	13.2 ± 0.2	12.3 ± 0.2	-1.0	-0.7	-0.7
GL564c	L4 ^c	12.5 ± 0.5	12.0 ± 0.5	11.0 ± 0.5	0.8	0.4	0.7
2MASS J0103+1935	L6 β	14.5 ± 0.4	13.3 ± 0.4	12.5 ± 0.4	-0.6	-0.3	-0.2
HD203030B	L7.5 ^c	15.0 ± 0.6	13.8 ± 0.2	13.1 ± 0.2	-0.8	-0.5	-0.5
HN Peg B	T2.5 ^c	14.5 ± 0.1	14.1 ± 0.1	13.8 ± 0.1	-0.1	-0.1	0.2

Notes.

^a Δ values are calculated from the MKO M_{JHK} values from the polynomials presented in Table 7. Negative values indicate underluminous objects.

^b 2MASS J0608-2753 is a member of the β Pictoris moving group as described in Rice et al. (2010).

^c Objects that are companions to young ($\ll 1$ Gyr) main-sequence stars.

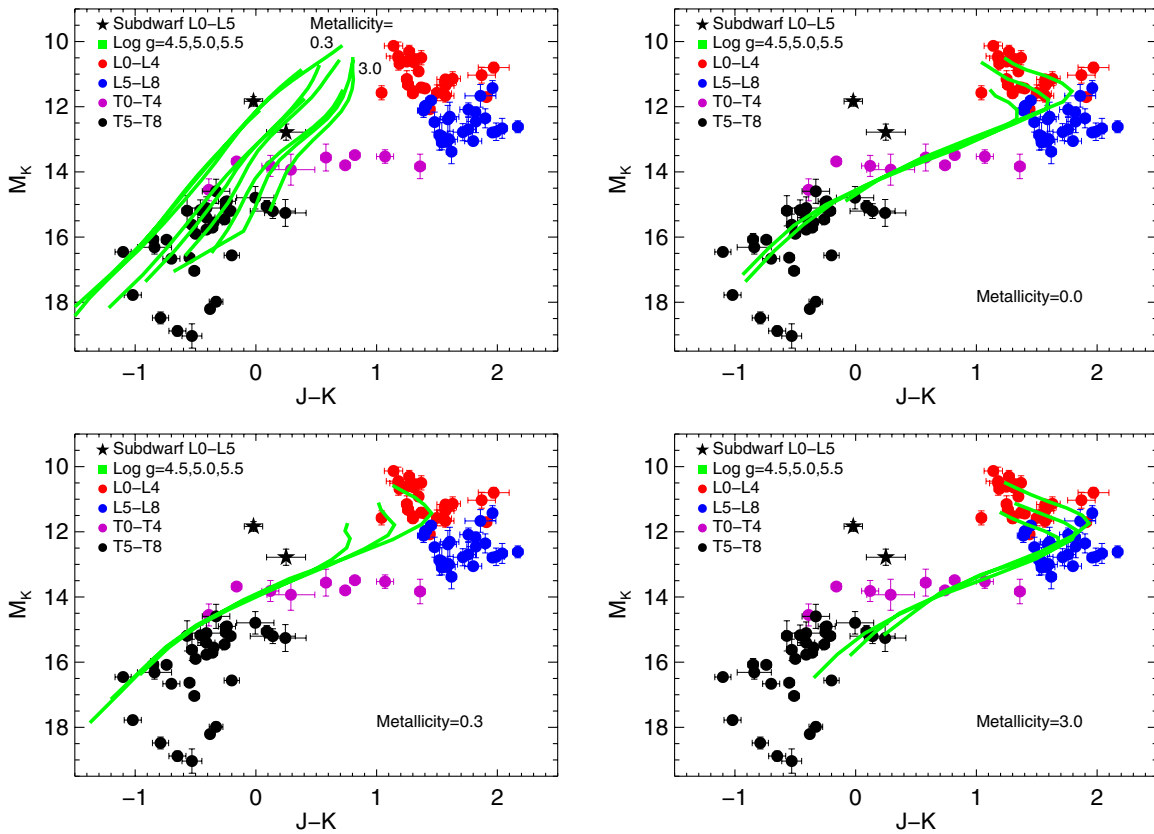


Figure 9. $J - K$ vs. M_K diagrams for L and T dwarfs with the evolutionary models of Burrows et al. (2006) overplotted. The top left panel shows the cloudless model with all metallicities and the remaining three panels show the cloudy model. Varying the metallicity from subsolar (0.0) to super-solar (3.0) and gravity from low ($\log(g) = 4.5$) to high ($\log(g) = 5.5$) fits the L and T dwarf sequences with varying degrees of accuracy.

(A color version of this figure is available in the online journal.)

The two latest-type L dwarfs in our sample are significantly redward of any of the Burrows et al. (2006) predictions but within the gravities explored on the cloudy model of Saumon & Marley (2008). Recent work by Barman et al. (2011) investigating HR8799b’s red near-IR color and relatively smooth near-IR spectrum concluded that thick photospheric dust cloud opacity could explain the planets observed luminosity and color. The latest-type L dwarfs in our sample may be higher mass analogs to HR 8799b (Barman et al. 2011).

7. SUBDWARFS

There are 12 ultracool subdwarfs with parallaxes including 8 late-type M and 4 L subdwarfs. Figure 13 shows the near-IR absolute magnitude versus spectral type diagrams for normal mid-type M through late-type L dwarfs (excluding binaries and low surface gravity dwarfs) with the subdwarfs overplotted. We show all subdwarfs including objects with absolute magnitude uncertainty >0.5 mag. As noted in Burgasser et al. (2008d), the L subdwarfs are overluminous in M_J but shift to normal or slightly underluminous by M_K . This has been attributed to reduced condensate opacity, as evidenced by strong TiO, Ca I, and Ti I features and enhanced collision-induced H_2 opacity at the K band (e.g., Ackerman & Marley 2001; Tsuji et al. 1996; Burgasser et al. 2003a, 2007). The effect is not as pronounced for the late-type M subdwarfs which, with the exception of SSSPM J1256–1408, appear at most slightly overluminous in M_J and normal or underluminous in M_H and M_K .

We compare photometry for the two L subdwarfs 2MASS J0532+8246 and 2MASS J1626+3925 in Figures 8 and 9. In Section 5.1, we find that early and mid-type L dwarfs are best fit by the cloudy tracks using both Saumon & Marley (2008) and Burrows et al. (2006) evolutionary models. However, variations in the metallicity of the cloudy tracks in Figure 9 do not reproduce the colors of the L subdwarfs. Instead, one must use the cloudless tracks supporting the idea that these objects are blue and overluminous at J due to reduced cloud opacity.

8. KINEMATICS

Combining the absolute parallax with the relative proper motion gives the tangential velocity (V_{tan}) of a source (see Table 2 for V_{tan} values of objects studied in this work). As our full astrometric sample is composed of objects in the immediate solar vicinity, V_{tan} values and their dispersions can be used as a rough indicator of age. In general, older objects will have had enough time to interact with objects in the Galactic disk and have their orbits perturbed while younger objects will retain a motion consistent with that of the Galactic disk (i.e., co-moving with their nascent cloud). The dispersion of a population is more informative than individual values for determining ages.

The median V_{tan} and σ_{tan} values for the 71 normal and unresolved binary L dwarfs with absolute magnitude uncertainties <0.5 are 27 km s $^{-1}$ and 20 km s $^{-1}$, respectively. For the 50 normal and unresolved binary T dwarfs we find similar values of 31 km s $^{-1}$ and 20 km s $^{-1}$, respectively. Our results are in good

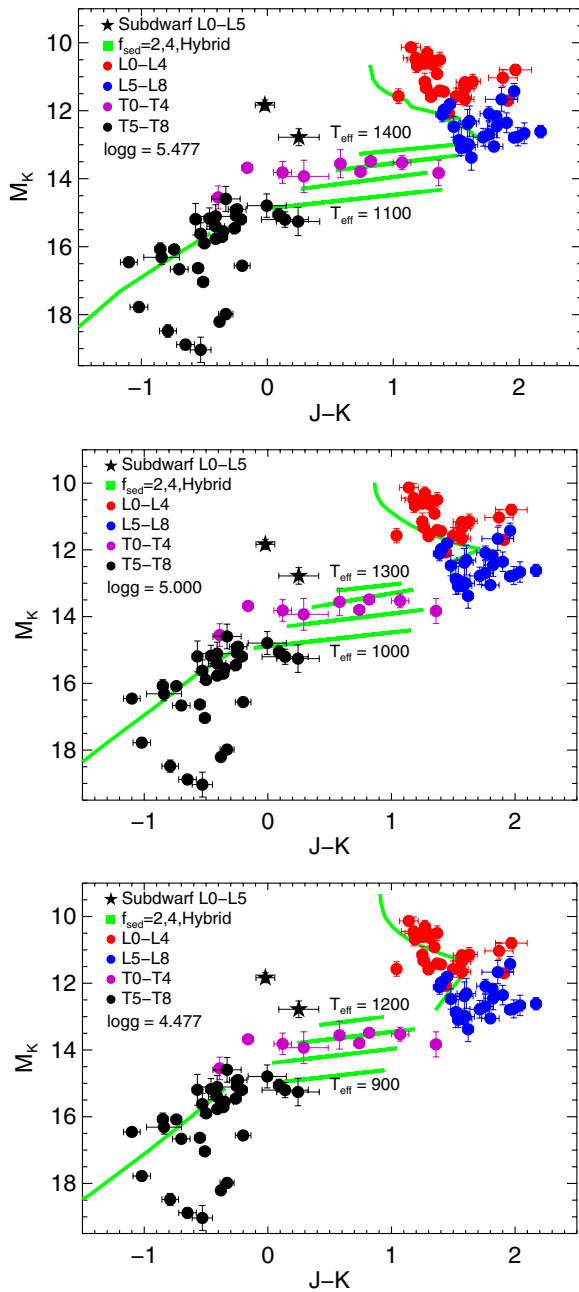


Figure 10. $J - K$ vs. M_K diagram for L and T dwarfs with the evolutionary models of Saumon & Marley (2008) overplotted to demonstrate the best fit for L/T transition objects. For late-type L dwarfs ($M_K < 13.0$) we have overplotted the $f_{\text{sed}} = 2$ tracks and for late-type T dwarfs ($M_K > 15.0$) we have overplotted the $f_{\text{sed}} = 4$ tracks. For the L/T transition we created a hybrid model between the two by adding the predicted model magnitudes of the latter to the former in 10% increments from $13.0 < M_K < 15.0$.

(A color version of this figure is available in the online journal.)

agreement with earlier population analyses (Faherty et al. 2009; Schmidt et al. 2010). Compared to the kinematic results of Vrba et al. (2004), we do not find a significant difference between the kinematics of L and T dwarfs. Based on the difference in dispersion between the L and T dwarfs, Vrba et al. (2004) concluded from their much smaller sample of UCDs that the L dwarfs were a kinematically younger population than the T dwarfs. In part, their conclusion was drawn from the fact that there were no T dwarfs with V_{tan} values $< 20 \text{ km s}^{-1}$. In our larger sample, we find 14 T dwarfs with V_{tan} values $< 20 \text{ km s}^{-1}$.

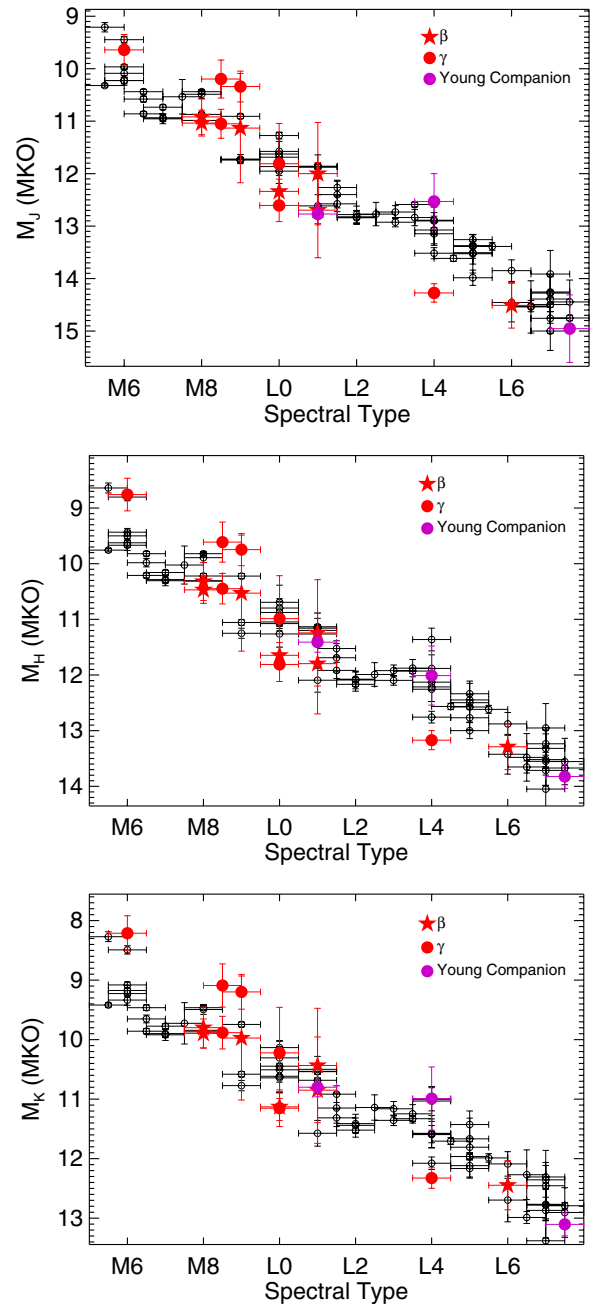


Figure 11. Spectral type vs. absolute magnitude in the MKO JHK filters for late-type M through mid-L dwarfs. Unfilled circles are normal dwarfs with parallax measurements. Red five point stars and filled circles are intermediate (β) and low (γ) surface gravity dwarfs, and purple filled circles are young ($\ll 1$ Gyr) companions to nearby stars. In Table 10, we report the difference in magnitude for each source from the M_{JHK} value calculated from the polynomials in Table 7. (A color version of this figure is available in the online journal.)

A two-sided K-S test on the L and T velocities yields a significant probability ($p \sim 0.33$) that the L and T dwarfs in our sample have identical kinematics hence ages.

We isolated the low surface gravity dwarfs and the subdwarfs and compared their kinematics to the overall sample (note that we have included late-type M dwarfs in each subset but only discuss objects whose absolute magnitude uncertainties are $< 0.5 \text{ mag}$). The former have significantly smaller V_{tan} values and tighter dispersions than the overall population and the latter significantly larger values. The median V_{tan} and σ_{tan}

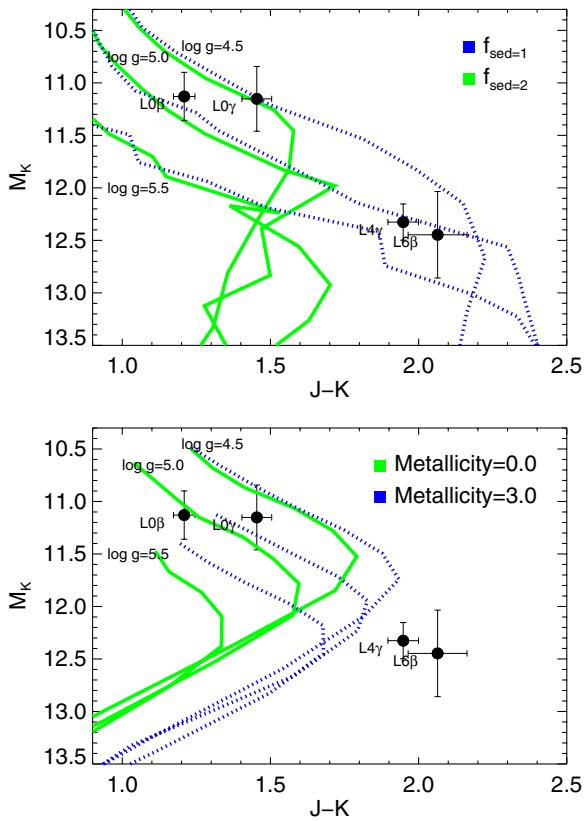


Figure 12. $J - K$ vs. M_K diagram with the evolutionary models of Saumon & Marley (2008; top panel) and Burrows et al (2006; bottom panel) overplotted along with four low surface gravity L dwarfs. The $\log(g) = [4.5, 5.0, 5.5]$ and $f_{\text{sed}} = 1, 2$ parameters of the former are shown as are the $\log(g) = [4.5, 5.0, 5.5]$, $\text{Metallicity} = [0.0, 3.0]$ parameters of the later.

(A color version of this figure is available in the online journal.)

values for the 10 low surface gravity dwarfs are 10 km s^{-1} and 14 km s^{-1} , respectively. For the nine subdwarfs, the median V_{tan} and σ_{tan} values are 241 km s^{-1} and 68 km s^{-1} , respectively. The considerable difference in values for each subset compared to the overall population further confirms expectations that they are younger (low surface gravity objects) and older (subdwarfs) than the overall UCD population.

9. BINARIES

When found as companions, brown dwarfs are primarily tightly bound (separations $< 20 \text{ AU}$) with a mass ratio close to 1 (e.g., Burgasser et al. 2003c; Close et al. 2003). As such, near-equal mass brown dwarf binaries can be identified on an H-R diagram by their overluminosity compared to equivalent spectral type objects. Moreover, if component photometry has been acquired one can investigate the properties of co-evolving systems and measure dynamical masses (e.g., Dupuy et al. 2009, 2008; Konopacky et al. 2010). Among the parallax sample listed in Table 5 there are 25 binaries unresolved in 2MASS. These are shown in Figure 3 as filled red circles.

There were four sources with parallaxes reported in this work with published high resolution imaging and predicted component spectral types from photometric data and/or spectral template fitting: 2M0518–2828, 2M1209–1004, 2M1404–3159, and 2M2052–1609. These four sources were used in the analysis of Section 4.1 and their system properties are listed in Table 6. When compared to the absolute magnitudes calculated for each spectral subtype using the polynomial reported in

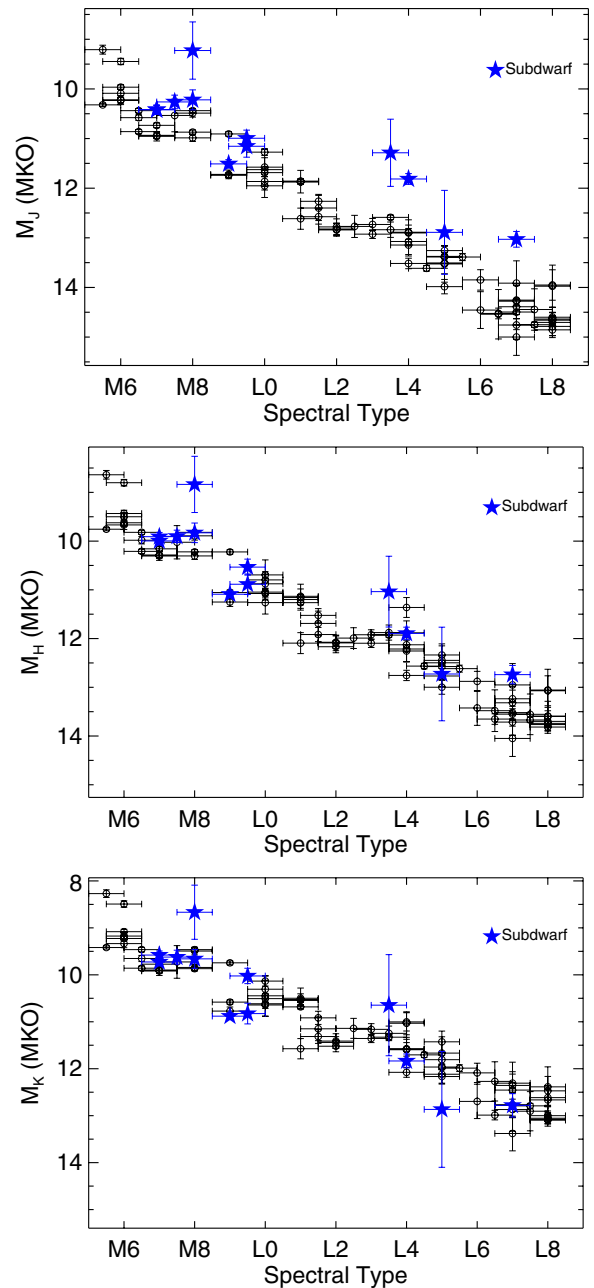


Figure 13. Spectral type vs. absolute magnitude in the MKO JHK filters for late-type M through L dwarfs. Unfilled circles are normal dwarfs with parallax measurements. Blue five point stars are subdwarfs with parallax measurements. (A color version of this figure is available in the online journal.)

Table 7, both components of 2M1209–1004, 2M2052–1609, and 2M0518–2828 fit within uncertainties on the brown dwarf main sequence. While the primary for 2M1404–3159 also fits within the brown dwarf main sequence, the T5 secondary is $\sim 1 \text{ mag}$ underluminous in M_{JHK} .

Burgasser et al. (2010a) used a template fitting technique to identify 17 new L–T transition binaries and three of the suspected binaries have parallaxes reported in this work: SDSS1511+0607, 2MASSJ0949–1545, and SDSS1207+0244. The first was regarded as a strong binary candidate while the latter two are weak binary candidates. Examining the H-R diagram in Figure 3 we find SDSS1511+0607 to be nearly 1 mag overluminous in M_{JHK} . C. R. Gelino et al. (in preparation) have followed up with Adaptive optics and resolved the two

components. We show both components in Figure 5 and list the individual magnitudes in Table 6. The proposed L5.5 and T5 components fit well within the brown dwarf main sequence.

Using new parallax measurements, 2MASSJ0949–1545 and SDSS1207+0244 fit well on the H-R diagram as single objects. If decomposed into the binary components proposed by Burgasser et al. (2010a), the primary and secondary sources would be >1 mag underluminous in multiple bands. We conclude that these sources are best treated as single sources.

10. CONCLUSIONS

We have measured parallaxes for 11 M, 32 L, and 27 T dwarfs in the local solar neighborhood. Nine calibrator stars were included in the sample to verify the reliability of our pipeline. The focus of this project was on low surface gravity dwarfs, L/T transition objects, and late-type T dwarfs within 20 pc of the Sun. The 70 new parallaxes significantly increase the number of brown dwarfs with accurate distance measurements.

We combined our sample with 115 literature measurements and used the full sample to re-define color–magnitude and spectrophotometric diagrams in *JHK*. Adding decomposed L/T transition binaries we find no reason to split spectral-type/absolute magnitude polynomials into “bright” and “faint” trends to account for unresolved binarity as has been done in the past. Isolating T0–T4 dwarfs to investigate the extent of the L/T transition brightening we find that there is a $[1.2\text{--}1.4]$ mag difference at *J*, $[0.3\text{--}0.5]$ mag difference at *H*, and a plateau or dimming of $[-0.2\text{ to }-0.3]$ mag at *K*. In agreement with flux reversal binary studies, this confirms the brightening—and the physical mechanism that drives it—as an intrinsic feature of brown dwarf atmospheric evolution.

We compared the $J - K$ versus M_K data for the full parallax sample to the evolutionary models of Saumon & Marley (2008) and Burrows et al. (2006). The $f_{\text{sed}} = 1, 2$ parameters best fit the L dwarf sequence and $f_{\text{sed}} = 4$ (corresponding to a very thin cloud layer) best fit the late-type T dwarf sequence using the Saumon & Marley (2008) models. The cloud model with varying gravity and metallicity reproduces the L dwarfs and the clear model with similar variations fits the T dwarfs using the Burrows et al. (2006) models. However, comparisons of both models to empirical data show significant red or potentially “ultra-cloudy” L dwarf outliers. Similarly there is significant scatter seen in the latest type T dwarfs that is unaccounted for in the clear and $f_{\text{sed}} = 4$ models indicating that condensate clouds continue to play a role in the photospheres of some low-temperature brown dwarfs. Investigations of individual objects in the “ultra-cloudy” sample reveals objects which are young/moderately young, implying a correlation between youth and enhanced photospheric dust.

No single f_{sed} parameter, gravity, nor metallicity track in the evolutionary models can account for the L/T transition objects. However, a hybrid model that smoothly transitions from $f_{\text{sed}} = 2$ (the best fit for late-type L dwarfs) to $f_{\text{sed}} = 4$ (the best fit for late-type T dwarfs) at a near-constant $T_{\text{eff}} = 1200 \pm 100$ K encompasses the majority of T0–T4 dwarfs. This temperature range is consistent with recent toy and sophisticated hybrid models but demonstrates that the range of spectral subtypes for which the temperature plateau is applicable is narrower than previously suspected (T0–T4 as opposed to L7–T4).

The low surface gravity objects with parallax measurements in this work are not explained by varying gravity in the evolutionary models. Rather, they appear to be underluminous compared to model color–magnitude diagrams and for their low

gravity spectral type. Among the 10 low surface gravity or young companion L dwarfs investigated, 80% appear $[0.2\text{--}1.0]$ mag underluminous for their spectral type in *J*, *H*, and/or *K*. Possible explanations for their underluminosity are that (1) the low-gravity and field dwarf spectral classification schemes are on different temperature scales with the low surface gravity objects intrinsically cooler than field age objects of the same type; and/or (2) young objects could have dustier photospheres than field-aged objects making them appear both fainter and redder.

A kinematic analysis of the astrometric sample reveals similar velocity dispersions between the L and T dwarf populations. A two-sided K-S test verifies that the two kinematic distributions are likely drawn from the same population and hence have similar age distributions. The low surface gravity and subdwarf samples have distinctly different velocity dispersions and are likely significantly younger and older (respectively) than normal objects.

We acknowledge the receipt of observation time through NOAO as well as the SMARTS consortium. Stony Brook’s participation in the SMARTS consortium is made possible by generous support by the Dean of Arts and Sciences, the Provost, and the Vice-President for Research of Stony Brook University. We thank the 4.0 m telescope operators C. Aguilera, M. Gonzalez, and A. Alvarez as well as 1.3 m observers A. Miranda, J. Espinoza, and J. Velasquez. J. K. Faherty gratefully acknowledges support from Hilary Lipsitz and from the AMNH and further acknowledges the encouragement and support made possible by Sahne Nuss during observing runs. This publication has made use of the Carnegie Astrometric Program parallax reduction software as well as the VLM Binaries Archive maintained by Nick Siegler at <http://www.vlmbinaries.org> and the data products from the Two Micron All-Sky Survey, which is a joint project of the University of Massachusetts and the Infrared Processing and Analysis Center/California Institute of Technology, funded by the National Aeronautics and Space Administration and the National Science Foundation. This research has made use of the NASA/IPAC Infrared Science Archive, which is operated by the Jet Propulsion Laboratory, California Institute of Technology, under contract with the National Aeronautics and Space Administration.

REFERENCES

- Ackerman, A. S., & Marley, M. S. 2001, *ApJ*, **556**, 872
- Allers, K. N., Liu, M. C., Dupuy, T. J., & Cushing, M. C. 2010, *ApJ*, **715**, 561
- Andreï, A. H., Smart, R. L., Penna, J. L., et al. 2011, *AJ*, **141**, 54
- Artigau, É., Radigan, J., Folkes, S., et al. 2010, *ApJ*, **718**, L38
- Barman, T. S., Macintosh, B., Konopacky, Q. M., & Marois, C. 2011, *ApJ*, **733**, 65
- Becklin, E. E., & Zuckerman, B. 1988, *Nature*, **336**, 656
- Biller, B. A., Kasper, M., Close, L. M., Brandner, W., & Kellner, S. 2006, *ApJ*, **641**, L141
- Boss, A. P., Weinberger, A. J., Anglada-Escudé, G., et al. 2009, *PASP*, **121**, 1218
- Bowler, B. P., Liu, M. C., & Cushing, M. C. 2009, *ApJ*, **706**, 1114
- Bowler, B. P., Liu, M. C., Dupuy, T. J., & Cushing, M. C. 2010, *ApJ*, **723**, 850
- Bowler, B. V., Liu, M. C., & Dupuy, T. J. 2010, *ApJ*, **710**, 45
- Burgasser, A. J. 2007, *AJ*, **134**, 1330
- Burgasser, A. J., Cruz, K. L., Cushing, M., et al. 2010a, *ApJ*, **710**, 1142
- Burgasser, A. J., Cruz, K. L., & Kirkpatrick, J. D. 2007, *ApJ*, **657**, 494
- Burgasser, A. J., Geballe, T. R., Leggett, S. K., Kirkpatrick, J. D., & Golimowski, D. A. 2006a, *ApJ*, **637**, 1067
- Burgasser, A. J., Kirkpatrick, J. D., Brown, M. E., et al. 1999, *ApJ*, **522**, L65
- Burgasser, A. J., Kirkpatrick, J. D., Brown, M. E., et al. 2002a, *ApJ*, **564**, 421
- Burgasser, A. J., Kirkpatrick, J. D., Burrows, A., et al. 2003a, *ApJ*, **592**, 1186
- Burgasser, A. J., Kirkpatrick, J. D., Cruz, K. L., et al. 2006b, *ApJS*, **166**, 585

- Burgasser, A. J., Kirkpatrick, J. D., Cutri, R. M., et al. 2000a, *ApJ*, **531**, L57
- Burgasser, A. J., Kirkpatrick, J. D., Liebert, J., & Burrows, A. 2003b, *ApJ*, **594**, 510
- Burgasser, A. J., Kirkpatrick, J. D., Reid, I. N., et al. 2003c, *ApJ*, **586**, 512
- Burgasser, A. J., Liu, M. C., Ireland, M. J., Cruz, K. L., & Dupuy, T. J. 2008a, *ApJ*, **681**, 579
- Burgasser, A. J., Looper, D. L., Kirkpatrick, J. D., Cruz, K. L., & Swift, B. J. 2008b, *ApJ*, **674**, 451
- Burgasser, A. J., Marley, M. S., Ackerman, A. S., et al. 2002b, *ApJ*, **571**, L151
- Burgasser, A. J., McElwain, M. W., & Kirkpatrick, J. D. 2003d, *AJ*, **126**, 2487
- Burgasser, A. J., McElwain, M. W., Kirkpatrick, J. D., et al. 2004, *AJ*, **127**, 2856
- Burgasser, A. J., Simcoe, R. A., Bochanski, J. J., et al. 2010b, *ApJ*, **725**, 1405
- Burgasser, A. J., Tinney, C. G., Cushing, M. C., et al. 2008c, *ApJ*, **689**, L53
- Burgasser, A. J., Vrba, F. J., Lépine, S., et al. 2008d, *ApJ*, **672**, 1159
- Burgasser, A. J., Wilson, J. C., Kirkpatrick, J. D., et al. 2000b, *AJ*, **120**, 1100
- Burgasser, A. J., Witte, S., Helling, C., et al. 2009, *ApJ*, **697**, 148
- Burningham, B., Leggett, S. K., Homeier, D., et al. 2011, *MNRAS*, **414**, 3590
- Burningham, B., Pinfield, D. J., Leggett, S. K., et al. 2008, *MNRAS*, **391**, 320
- Burningham, B., Pinfield, D. J., Leggett, S. K., et al. 2009, *MNRAS*, **395**, 1237
- Burrows, A., Hubbard, W. B., Lunine, J. I., & Liebert, J. 2001, *Rev. Mod. Phys.*, **73**, 719
- Burrows, A., Hubbard, W. B., Lunine, J. I., et al. 1997, in ASP Conf. Ser. 119, Planets Beyond the Solar System and the Next Generation of Space Missions, ed. D. Soderblom (San Francisco, CA: ASP), 9
- Burrows, A., Sudarsky, D., & Hubeny, I. 2006, *ApJ*, **640**, 1063
- Carpenter, J. M. 2001, *AJ*, **121**, 2851
- Chabrier, G., & Baraffe, I. 1997, *A&A*, **327**, 1039
- Chauvin, G., Lagrange, A.-M., Zuckerman, B., et al. 2005, *A&A*, **438**, L29
- Chiu, K., Fan, X., Leggett, S. K., et al. 2006, *AJ*, **131**, 2722
- Close, L. M., Siegler, N., Freed, M., & Biller, B. 2003, *ApJ*, **587**, 407
- Costa, E., Méndez, R. A., Jao, W.-C., et al. 2005, *AJ*, **130**, 337
- Costa, E., Méndez, R. A., Jao, W.-C., et al. 2006, *AJ*, **132**, 1234
- Cruz, K. L., Burgasser, A. J., Reid, I. N., & Liebert, J. 2004, *ApJ*, **604**, L61
- Cruz, K. L., Kirkpatrick, J. D., & Burgasser, A. J. 2009, *AJ*, **137**, 3345
- Cruz, K. L., Reid, I. N., Kirkpatrick, J. D., et al. 2007, *AJ*, **133**, 439
- Cruz, K. L., Reid, I. N., Liebert, J., Kirkpatrick, J. D., & Lowrance, P. J. 2003, *AJ*, **126**, 2421
- Currie, T., Burrows, A., Itoh, Y., et al. 2011, *ApJ*, **729**, 128
- Cushing, M. C., Kirkpatrick, J. D., Gelino, C. R., et al. 2011, *ApJ*, **743**, 50
- Cushing, M. C., Looper, D., Burgasser, A. J., et al. 2009, *ApJ*, **696**, 986
- Dahn, C. C., Harris, H. C., Vrba, F. J., et al. 2002, *AJ*, **124**, 1170
- Delfosse, X., Tinney, C. G., Forveille, T., et al. 1997, *A&A*, **327**, L25
- Delfosse, X., Tinney, C. G., Forveille, T., et al. 1999, *A&AS*, **135**, 41
- Delorme, P., Albert, L., Forveille, T., et al. 2010, *A&A*, **518**, 39
- Delorme, P., Delfosse, X., Albert, L., et al. 2008, *A&A*, **482**, 961
- Dupuy, T. J., Liu, M. C., & Bowler, B. P. 2009, *ApJ*, **706**, 328
- Dupuy, T. J., Liu, M. C., & Ireland, M. J. 2008, arXiv e-prints
- Ellis, S. C., Tinney, C. G., Burgasser, A. J., Kirkpatrick, J. D., & McElwain, M. W. 2005, *AJ*, **130**, 2347
- EROS Collaboration, Goldman, B., Delfosse, X., Forveille, T., et al. 1999, *A&A*, **351**, L5
- Faherty, J. K., Burgasser, A. J., Bochanski, J. J., et al. 2011, *AJ*, **141**, 71
- Faherty, J. K., Burgasser, A. J., Cruz, K. L., et al. 2009, *AJ*, **137**, 1
- Faherty, J. K., Burgasser, A. J., West, A. A., et al. 2010, *AJ*, **139**, 176
- Fan, X., Knapp, G. R., Strauss, M. A., et al. 2000, *AJ*, **119**, 928
- Forveille, T., Ségransan, D., Delorme, P., et al. 2004, *A&A*, **427**, L1
- Geballe, T. R., Knapp, G. R., Leggett, S. K., et al. 2002, *ApJ*, **564**, 466
- Gizis, J. E., Monet, D. G., Reid, I. N., et al. 2000, *AJ*, **120**, 1085
- Gizis, J. E., Reid, I. N., Knapp, G. R., et al. 2003, *AJ*, **125**, 3302
- Goldman, B., Marsat, S., Henning, T., Clemens, C., & Greiner, J. 2010, *MNRAS*, **405**, 1140
- Golimowski, D. A., Leggett, S. K., Marley, M. S., et al. 2004, *AJ*, **127**, 3516
- Goto, M., Kobayashi, N., Terada, H., et al. 2002, *ApJ*, **567**, L59
- Harrington, R. S., & Dahn, C. C. 1980, *AJ*, **85**, 454
- Hawley, S. L., Covey, K. R., Knapp, G. R., et al. 2002, *AJ*, **123**, 3409
- Hayashi, C., & Nakano, T. 1963, *Prog. Theor. Phys.*, **30**, 460
- Helling, C., Ackerman, A., Allard, F., et al. 2008, *MNRAS*, **391**, 1854
- Henry, T. J., Jao, W.-C., Subasavage, J. P., et al. 2006, *AJ*, **132**, 2360
- Hog, E., Fabricius, C., Makarov, V. V., et al. 2000, VizieR Online Data Catalog, **1259**, 0
- Jao, W., Henry, T. J., Subasavage, J. P., et al. 2005, *AJ*, **129**, 1954
- Kasper, M., Biller, B. A., Burrows, A., et al. 2007, *A&A*, **471**, 655
- Kendall, T. R., Delfosse, X., Martín, E. L., & Forveille, T. 2004, *A&A*, **416**, L17
- Kirkpatrick, J. D. 2005, *ARA&A*, **43**, 195
- Kirkpatrick, J. D., Barman, T. S., Burgasser, A. J., et al. 2006, *ApJ*, **639**, 1120
- Kirkpatrick, J. D., Beichman, C. A., & Skrutskie, M. F. 1997, *ApJ*, **476**, 311
- Kirkpatrick, J. D., Cruz, K. L., Barman, T. S., et al. 2008, *ApJ*, **689**, 1295
- Kirkpatrick, J. D., Dahn, C. C., Monet, D. G., et al. 2001, *AJ*, **121**, 3235
- Kirkpatrick, J. D., Looper, D. L., Burgasser, A. J., et al. 2010, *ApJS*, **190**, 100
- Kirkpatrick, J. D., Reid, I. N., Liebert, J., et al. 1999, *ApJ*, **519**, 802
- Kirkpatrick, J. D., Reid, I. N., Liebert, J., et al. 2000, *AJ*, **120**, 447
- Kitchin, C. R. 1976, Allen's Astrophysical Quantities, ed. Arthur N. Cox (London: The Athlone Press)
- Knapp, G. R., Leggett, S. K., Fan, X., et al. 2004, *AJ*, **127**, 3553
- Konopacky, Q. M., Ghez, A. M., Barman, T. S., et al. 2010, *ApJ*, **711**, 1087
- Koornneef, J. 1983, *A&A*, **128**, 84
- Kumar, S. S. 1962, *AJ*, **67**, 579
- Leggett, S. K., Allard, F., Dahn, C., et al. 2000, *ApJ*, **535**, 965
- Leggett, S. K., Burningham, B., Saumon, D., et al. 2010, *ApJ*, **710**, 1627
- Lépine, S., Rich, R. M., & Shara, M. M. 2003a, *ApJ*, **591**, L49
- Lépine, S., Rich, R. M., & Shara, M. M. 2003b, *AJ*, **125**, 1598
- Lépine, S., Shara, M. M., & Rich, R. M. 2003c, *ApJ*, **585**, L69
- Liu, M. C., Deacon, N. R., Magnier, E. A., et al. 2011, *ApJ*, **740**, L32
- Liu, M. C., Delorme, P., Dupuy, T. J., et al. 2011, *ApJ*, **740**, L108
- Liu, M. C., Dupuy, T. J., & Leggett, S. K. 2010, *ApJ*, **722**, 311
- Liu, M. C., Leggett, S. K., Golimowski, D. A., et al. 2006, *ApJ*, **647**, 1393
- Lodieu, N., Pinfield, D. J., Leggett, S. K., et al. 2007, *MNRAS*, **379**, 1423
- Looper, D. L., Gelino, C. R., Burgasser, A. J., & Kirkpatrick, J. D. 2008a, *ApJ*, **685**, 1183
- Looper, D. L., Kirkpatrick, J. D., & Burgasser, A. J. 2007, *AJ*, **134**, 1162
- Looper, D. L., Kirkpatrick, J. D., Cutri, R. M., et al. 2008b, *ApJ*, **686**, 528
- Lucas, P. W., Tinney, C. G., Burningham, B., et al. 2010, *MNRAS*, **408**, L56
- Luhman, K. L., Patten, B. M., Marengo, M., et al. 2007, *ApJ*, **654**, 570
- Marley, M. S., Saumon, D., & Goldblatt, C. 2010, *ApJ*, **723**, L117
- Marocco, F., Smart, R. L., Jones, H. R. A., et al. 2010, *A&A*, **524**, A38
- Martin, E. L., Brandner, W., & Basri, G. 1999, *Science*, **283**, 1718
- McCaughrean, M. J., Close, L. M., Scholz, R.-D., et al. 2004, *A&A*, **413**, 1029
- Metchev, S. A., & Hillenbrand, L. A. 2004, *ApJ*, **617**, 1330
- Metchev, S. A., & Hillenbrand, L. A. 2006, *ApJ*, **651**, 1166
- Monet, D. G., Dahn, C. C., Vrba, F. J., et al. 1992, *AJ*, **103**, 638
- Mugrauer, M., Seifahrt, A., Neuhäuser, R., & Mazeh, T. 2006, *MNRAS*, **373**, L31
- Nakajima, T., Oppenheimer, B. R., Kulkarni, S. R., et al. 1995, *Nature*, **378**, 463
- Patten, B. M., Stauffer, J. R., Burrows, A., et al. 2006, *ApJ*, **651**, 502
- Perryman, M. A. C., Lindegren, L., Kovalevsky, J., et al. 1997, *A&A*, **323**, L49
- Phan-Bao, N., Bessell, M. S., Martín, E. L., et al. 2006, *MNRAS*, **366**, L40
- Pinfield, D. J., Burningham, B., Tamara, M., et al. 2008, *MNRAS*, **390**, 304
- Potter, D., Martín, E. L., Cushing, M. C., et al. 2002, *ApJ*, **567**, L133
- Radigan, J., Jayawardhana, R., Lafrenière, D., et al. 2012, *ApJ*, **750**, 105
- Rebolo, R., Zapatero Osorio, M. R., & Martín, E. L. 1995, *Nature*, **377**, 129
- Reid, I. N., & Cruz, K. L. 2002, *AJ*, **123**, 2806
- Reid, I. N., Cruz, K. L., Kirkpatrick, J. D., et al. 2008, *AJ*, **136**, 1290
- Reid, I. N., Hawley, S. L., & Gizis, J. E. 1995, *AJ*, **110**, 1838
- Reid, I. N., Kirkpatrick, J. D., Gizis, J. E., et al. 2000, *AJ*, **119**, 369
- Rice, E. L., Faherty, J. K., & Cruz, K. L. 2010, *ApJ*, **715**, L165
- Ruiz, M. T., Leggett, S. K., & Allard, F. 1997, *ApJ*, **491**, L107
- Saumon, D., Hubbard, W. B., Burrows, A., et al. 1996, *ApJ*, **460**, 993
- Saumon, D., & Marley, M. S. 2008, *ApJ*, **689**, 1327
- Schilbach, E., Röser, S., & Scholz, R. 2009, *A&A*, **493**, L27
- Schmidt, S. J., West, A. A., Burgasser, A. J., Bochanski, J. J., & Hawley, S. L. 2010, *AJ*, **139**, 1045
- Schmidt, S. J., West, A. A., Hawley, S. L., & Pineda, J. S. 2010, *AJ*, **139**, 1808
- Schneider, D. P., Knapp, G. R., Hawley, S. L., et al. 2002, *AJ*, **123**, 458
- Scholz, R., Lehmann, I., Matute, I., & Zinnecker, H. 2004a, *A&A*, **425**, 519
- Scholz, R., Lodieu, N., & McCaughrean, M. J. 2004b, *A&A*, **428**, L25
- Scholz, R. D. 2010, *A&A*, **510**, L8
- Scholz, R.-D., McCaughrean, M. J., Lodieu, N., & Kuhlbrodt, B. 2003, *A&A*, **398**, L29
- Siegler, N., Close, L. M., Burgasser, A. J., et al. 2007, *AJ*, **133**, 2320
- Sivarani, T., Lépine, S., Kembhavi, A. K., & Gupchup, J. 2009, *ApJ*, **694**, L140
- Stephens, D. C., & Leggett, S. K. 2004, *PASP*, **116**, 9
- Stone, R. C. 1996, *PASP*, **108**, 1051
- Stone, R. C. 2002, *PASP*, **114**, 1070
- Strauss, M. A., Fan, X., Gunn, J. E., et al. 1999, *ApJ*, **522**, L61
- Stumpf, M. B., Brandner, W., Henning, T., et al. 2008, arXiv e-prints
- Stumpf, M. B., Geißler, K., Bouy, H., et al. 2011, *A&A*, **525**, A123
- Teixeira, R., Ducourant, C., Chauvin, G., et al. 2008, *A&A*, **489**, 825
- Thorstensen, J. R., & Kirkpatrick, J. D. 2003, *PASP*, **115**, 1207
- Tinney, C. G., Burgasser, A. J., & Kirkpatrick, J. D. 2003, *AJ*, **126**, 975
- Tinney, C. G., Burgasser, A. J., Kirkpatrick, J. D., & McElwain, M. W. 2005, *AJ*, **130**, 2326
- Tokunaga, A. T., Simons, D. A., & Vacca, W. D. 2002, *PASP*, **114**, 180
- Tsuji, T., & Nakajima, T. 2003, *ApJ*, **585**, L151

- Tsuji, T., Ohnaka, K., Aoki, W., & Nakajima, T. 1996, *A&A*, **308**, [L29](#)
- Tsvetanov, Z. I., Golimowski, D. A., Zheng, W., et al. 2000, *ApJ*, **531**, [L61](#)
- Tukey, J. W. 1977, *Exploratory Data Analysis* (Addison-Wesley Series in Behavioral Science: Quantitative Methods) (Reading, Mass.: Addison-Wesley)
- van Altena, W. F., Lee, J. T., & Hoffleit, E. D. 1995, *The General Catalogue of Trigonometric [Stellar] Parallaxes* (4th ed.; New Haven, CT: Yale Univ. Observatory)
- van Leeuwen, F. (ed.) 2007, *A&A*, **474**, [653](#)
- van der Blik, N. S., Norman, D., Blum, R. D., et al. 2004, *Proc. SPIE*, **5492**, [1582](#)
- Vrba, F. J., Henden, A. A., Luginbuhl, C. B., et al. 2004, *AJ*, **127**, [2948](#)
- Wahhaj, Z., Liu, M. C., Biller, B. A., et al. 2011, *ApJ*, **729**, [139](#)
- Warren, S. J., Mortlock, D. J., Leggett, S. K., et al. 2007, *MNRAS*, **381**, [1400](#)
- Wilson, J. C., Kirkpatrick, J. D., Gizis, J. E., et al. 2001, *AJ*, **122**, [1989](#)